

**VISUALIZATION OF NUCLEATION OF SUPERCRITICAL
CARBON DIOXIDE FLOW THROUGH A NOZZLE**

A Thesis
Presented to
The Academic Faculty

by

Chang Hyeon Lim

In Partial Fulfillment
of the Requirements for
Master of Science in the School of Mechanical Engineering

Georgia Institute of Technology
May 2019

COPYRIGHT © 2019 BY CHANG HYEON LIM

VISUALIZATION OF NUCLEATION OF SUPERCRITICAL CARBON DIOXIDE FLOW THROUGH A NOZZLE

Approved by:

Dr. Devesh Ranjan, Advisor
School of Mechanical Engineering
Georgia Institute of Technology

Dr. Peter Loutzenhiser
School of Mechanical Engineering
Georgia Institute of Technology

Dr. Wenting Sun
School of Aerospace Engineering
Georgia Institute of Technology

Date Approved: April 18, 2019

ACKNOWLEDGEMENTS

I would like to show my appreciation to Dr. Devesh Ranjan and my colleagues of Shock Tube and Advanced Mixing Lab who made it possible for this thesis to come along as one piece. I would also like to thank my thesis committee Dr. Peter Loutzenhiser and Dr. Wenting Sun for valuable feedback. Special thanks to the CO₂ group of the lab (Sandeep Pidaparti, Taegyu Kang, and Alon Katz) who have given indefinite input for me to conduct an experiment. I am also grateful to Dr. Svyatoslav Yorish, Robert (Shane) Getchell, and Henry (Chris) Balance who have helped me to make this experiment possible and safe. Above all, I would like to thank my parents and my sister for moral support and encouragement.

TABLE OF CONTENTS

ACKNOWLEDGEMENTS	iii
LIST OF TABLES	vi
LIST OF FIGURES	vii
LIST OF SYMBOLS AND ABBREVIATIONS	ix
SUMMARY	xii
CHAPTER 1. Introduction	1
1.1 Background of supercritical CO ₂ power cycles	1
1.2 Motivation and previous nucleation studies	2
1.3 Objectives	6
CHAPTER 2. Experimental facility and system	8
2.1 Flow control equipment	8
2.1.1 Hydropac CO ₂ compressor	8
2.1.2 High/low pressure accumulator	9
2.1.3 Heating/cooling components	10
2.1.4 Flow rate controlling needle valve	10
2.2 Test Section	11
2.3 Instrumentation	14
2.4 Safety Features	15
2.5 High speed direct shadowgraphy	16
CHAPTER 3. Experimental Procedure and Operation	18
3.1 Pre-experimental setup	18
3.2 Experimental procedure	19
3.3 Experiment closure procedure	21
CHAPTER 4. Theoretical Calculation and Experimental Results	22
4.1 Theoretical model calculation and comparison	23
4.2 Visualization of non-equilibrium condensation	29
CHAPTER 5. Conclusion and Future Work	36
5.1 Conclusion	36
5.2 Future work	36
5.2.1 Closed-loop facility and test section	36
5.2.2 Non-intrusive measurement using orthogonal optical access	38
5.2.3 Development of stochastic model in condensation behavior	38
APPENDIX A. Safety Operating Procedure	39
APPENDIX B. List of Loop component specifications	41

APPENDIX C. Tube Wall thickness calculation	42
APPENDIX D. Window wall thickness calculation	43
APPENDIX E. Experimental Data	44
APPENDIX F. Test Section and heater assembly	45
APPENDIX G. Flow coefficient calculation	47
APPENDIX H. Data acquisition labview code	49
APPENDIX I. Condensation Analysis using Matlab	52
APPENDIX J. Homogeneous equilibrium model code	55
APPENDIX K. Nozzle Dimensions	59
APPENDIX L. Improvements to the Facility	60
REFERENCES	63

LIST OF TABLES

Table 1	Accuracy of instrumentation used in the experimental facility	15
Table 2	Experimental conditions at the inlet of the test section	22
Table 3	minimum tube wall thickness calculation	42
Table 4	minimum sapphire glass window wall calculation	43
Table 5	Experimental data for Run #1 and #2	44
Table 6	Flow coefficient calculation for flow controlling valves	47

LIST OF FIGURES

Figure 1:	T-s diagram of inlet, throat, and exit conditions of a nozzle presented by C. Lettieri	4
Figure 2:	Non-equilibrium throat condensation conditions presented in thesis by Derek Paxon	4
Figure 3:	Shadowgraph-like (a) instantaneous image of the channel flow, (b) background image and (c) normalized intensity image	5
Figure 4:	Compressor inlet and converging point conditions	7
Figure 5:	(top) 3D model of experimental facility and (bottom) 2D schematics of experimental facility with flow direction	9
Figure 6:	Actual experimental setup images with facility components	11
Figure 7:	Flow profile geometry with pressure transducer locations	12
Figure 8:	O-ring location on nozzle face and bottom flange face	13
Figure 9:	Schematic of the high-speed direct shadowgraphy setup (test section flow is into the page)	16
Figure 10:	Phase transition images of different flows	17
Figure 11:	Side view of experimental facility with flow direction	18
Figure 12:	Experimental test conditions on T-s diagram	23
Figure 15:	Comparison between homogeneous equilibrium model and experimental data for (top) run #1 (bottom) run #2 of test conditions	28
Figure 13:	Comparison of void fractions (left) on central plane and (right) on the wall plane of the flow profile	26
Figure 16:	Indication of recirculation zone in velocity field vector along the flow profile [15]	29
Figure 17:	Development of non-equilibrium condensation as it reaches	30
Figure 18:	a) Instantaneous raw shadowgraph, and (b) average, and (c) variance of β . Lines 1-5 in (b) indicate locations where $\phi\beta$ was computed	31
Figure 19:	Image processing steps for relative void fractions	33

Figure 20:	Power spectral density, $\phi\beta$, over five different locations marked in Figure 18(b)	33
Figure 21:	Two example sets of images [(a) and (b), (c) and (d)] for successive frames of condensation separated by $1/\text{fs}$	35
Figure 22:	Nozzle geometry variations for different flow regime	37
Figure 23:	Order of valves opening before the experiment	39
Figure 24:	Order of valves closing after the experiment	40
Figure 25:	Exploded isometric view of test section	45
Figure 26:	Isometric and side view of heater assembly	46
Figure 27:	Flow coefficient chart for (left) SS-8GUF8 and (right) SS-5PDF8 [26], [27]	48
Figure 28:	Nozzle dimensions and locations of pressure transducers	59
Figure 29:	(Left) Previous experimental setup with 5 gallons of LP accumulator (Right) current experimental setup with 30 gallons of LP accumulator	60
Figure 30:	Front views of test section flanges before and after o-ring groove installation	61
Figure 31:	(Top) Wire diagram of the flow guidance insert (Bottom) Test section inlet cross-sectional image of before and after installation of flow guidance insert	62

LIST OF SYMBOLS AND ABBREVIATIONS

Abbreviation

AS	allowable stress, psia
CA	corrosion allowance, in
CCS	Carbon Capture and Storage
DP	Design pressure, psia
EOR	Enhanced oil recover
FOS	factor of safety
HEM	Homogeneous Equilibrium Model
HP	High pressure
JF	joint factor
LP	Low pressure
OD	outside diameter, in
T_{\min}	minimum thickness, in
Y	wall thickness coefficient

Greek Symbols

β	Relative volume fraction
ρ	Density, kg/m ³
Φ_B	Pre-multiplied power spectra
τ	Time scale, s
ν	Viscosity, kg/m-s

Mathematical Symbols

A	Nozzle cross-sectional area, m ²
-----	---

f_s	Shedding frequency, 1/s
h	Enthalpy, J/kg
H	Characteristic height in cross-section, mm
J_{\max}	Maximum nucleation rate, m ³ /s
K_w	Support condition constant
l	Characteristic length in nozzle, mm
L_w	Unsupported length, mm
m	Mass, kg
\dot{m}	Mass flow rate, kg/s
P	Pressure, MPa
Q	Heat, J
s	Entropy, J/kg-K
S_f	Fracture strength of material, MPa
T	Temperature, K
t	Time, s
V	Velocity, m/s
\mathbb{V}	Volume, m ³
W	Work, J
y	Normal direction to bottom wall

Subscripts

0	Inlet/Stagnation condition
avg	Average
g	Gas phase
i	i-th cross-section element in the nozzle
in	internal

- l Liquid phase
- m Two-phase mixture
- o Outer or ambient

SUMMARY

Interest in fundamental properties of carbon dioxide near the critical point led to an investigation of supercritical CO₂ flow through a converging-diverging nozzle. To study a phase change and flow behavior of supercritical CO₂ flow, a closed-loop carbon dioxide loop is built with an optically accessible test section. Unlike previous studies in which most of the experiment were performed in a blowdown facility, a steady-state closed loop is built to visually inspect the nucleation behavior of carbon dioxide near the critical point. In addition, a high-speed optical diagnostic is performed on the test section to interpret the nucleation behavior at temporal resolution on the order of microsecond. Three different parameters (pressure, temperature, and flow rate) for the supercritical flow are controlled for a provided converging-diverging nozzle geometry. Theoretical flow calculation using a homogeneous equilibrium model is computed and compared with the experimentally observed flow properties. With the high-speed diagnostics, the specific geometry yields a dominant shedding frequency that governs the flow behavior near the critical point.

CHAPTER 1. INTRODUCTION

1.1 Background of supercritical CO₂ power cycles

With a rise in environmental awareness, significant attention is given to a new candidate of working fluid in thermodynamic power cycles: carbon dioxide. Non-reactive gas that is a common byproduct of a chemical reaction, carbon dioxide has merits of high density and heat capacity near the critical point compared to other working fluids. These advantages allow the supercritical CO₂ power cycle to be more efficient, and to have reduced turbomachinery size compared to the traditional Rankine cycle. This new power cycle technology could be applicable where power generation is required in a confined space. The power cycle can also be utilized in next generation nuclear reactors to provide stability and safety of the overall system and maintain high operating temperatures up to 900°C [1]. A sCO₂ cycle coupled to a Sodium-cooled Fast Reactor can increase safety of the plant by avoiding potentially dangerous sodium-water interactions in steam-based cycles. Moreover, a supercritical carbon dioxide power cycle can be utilized in exhaust/waste heat recovery when downstream of the sCO₂-turbines is greater than 450°C [1]. Carbon capture and storage technology (CCS) is developed to capture carbon dioxide from combustion products that will otherwise be emitted to the atmosphere. The captured carbon dioxide is compressed and stored in a geological reservoir to reduce greenhouse gas emissions or used for enhanced oil recovery (EOR) [2], [3]. All these advancements rooted from Dostal [4] who modeled a supercritical carbon dioxide cycle and presented the possibility of future power cycles that can be substituted for the traditional steam-based Rankine cycle. Taking advantage of these beneficial high density and heat capacity comes

with a great challenge: compression and expansion work near the critical point can lead to unstable conditions if not properly controlled.

1.2 Motivation and previous nucleation studies

Compression and expansion work near the critical point pose a risk of phase transition, which introduces two-phase flow effects to the flow dynamics and inner components of the compressor. Inception of nucleation due to the phase change yields detrimental effects to the overall compressor performance. Chaitanya Halbe presented in his thesis that the phase change occurring in a multi-stage compressor is sufficient to pose a decrease in performance and degradation in component materials of the compressor [5]. Though the investigated working fluid is R-134a, it underscores a concern of the two-phase flow impact on any compressor that is subjected to phase transition during compression work. Specifically in carbon dioxide, one of the earliest works of a nozzle flow study dates back to 1966 by Karl Duff [6], who studied non-equilibrium carbon dioxide condensation in a De Laval nozzle with variable expansion rates. An important conclusion from the work was that the carbon dioxide flow through a nozzle can be considered one dimensional isentropic flow due to the small boundary layers that were observed by interferometry in the tested nozzle geometry. While the experimental results were able to generate similar trends, the exact property changes according to the classical nucleation theory were not able to be reproduced. A similar study was done more recently by Lettieri et al. [[7],[8]] who conducted a more thorough experimental study was performed using a shearing interferometry technique to construct the density field map along the nozzle profile. Shearing interferometry allows the quantitative analysis of density measurements along the nozzle. Density and pressure measurements were experimentally obtained at the

condensation front for different inlet conditions. These measurements became the basis of the extrapolation of the Wilson line on the metastable regions. Numerical calculations using Span and Wagner's Equation of State model for pressure and density along the profile were compared to the experimental results and concluded that the model can accurately predict the carbon dioxide properties at metastable regions [9]. Further experimental studies of supercritical carbon dioxide flow through a nozzle are done for ejector applications in CO₂ refrigeration cycles. Trans-critical carbon dioxide cycle studies by Fang et al. [10] showed the presence of significant impact of nozzle geometry to its ejector performance by experimentally studying the relation between motive and suction inlet pressure ratios, diameter ratios, and mixing length. Nakagawa et al. [11] have done experiments with similar scope, but instead of using an actual ejector, a nozzle with four different angles was tested to observe the nucleation effects. Pressure and temperature profiles along the nozzle were recorded and compared with the isentropic homogeneous equilibrium theory. The experimental data and the isentropic homogeneous equilibrium theory agreed well as the divergence angle grew larger with higher inlet temperature. Apart from experiments, the nucleation in sCO₂ flows in nozzles has been investigated in numerical studies. A computational study done by A. Hosagandi et al. explored phase transition phenomena based on different inlet conditions of the CO₂ compressor. From the study, variations in the inlet conditions resulted in two different two-phase phenomena: condensation and cavitation. A. Hosagandi showed from calculation that the two-phase flow phenomena are not considered significant to the compressor performance or material of components as the density or pressure ratios are not tremendous [13]. Ameli et al. in his computational work pointed out a potential for erosion of the compressor component

material through calculation of skin friction loss [14]. Jarrahbashi et al. [15] performed a transient supercritical carbon dioxide flow through a converging-diverging nozzle profile using OpenFOAM and analyzed the nucleation rate along the nozzle profile.

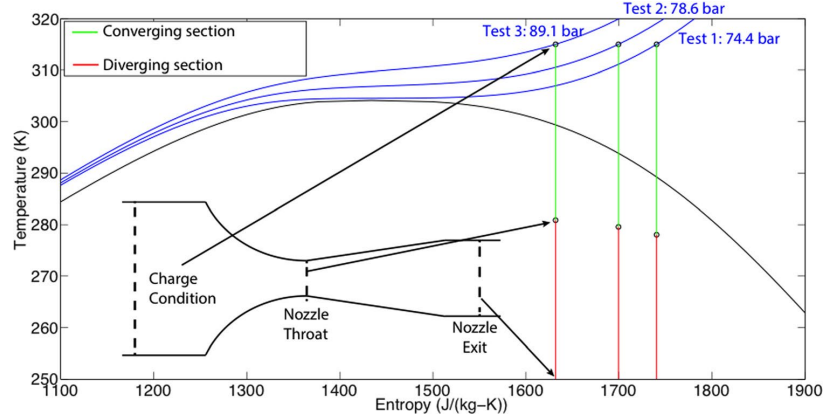


Figure 1: T-s diagram of inlet, throat, and exit conditions of a nozzle presented by C. Lettieri [8]

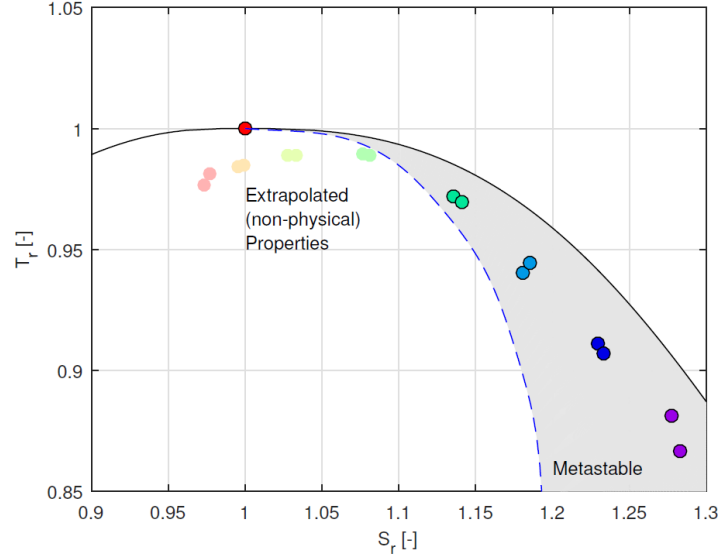


Figure 2: Non-equilibrium throat condensation conditions presented in thesis by Derek Paxson [16]

Previous works listed from [6-11] require a gas flow from inlet to outlet of the test section at high mass flowrate to observe condensing behavior of a fluid flow. Most of these

experimental setups are pressure-driven flow with one charged tank connected in series to a test section. Observing cavitation requires a liquid flow through the test section with an abrupt pressure change to inspect a sudden increase of gaseous phase in the bulk fluid. Rather than a pressure-driven flow, pumps are utilized to direct a constant flow through the test section. Reboud et al. [17] had a closed loop of water passing through a venturi nozzle for investigation of cavitating water flow. The work shows shedding frequency observation that is governed by a dominant frequency through power spectral density. Recent work can be found by Mauger et al. [18] who used a pump, metal sheets, and glass window to visually observe the cavitation of testing oil (ISO 4113). Mauger expresses cavitating flow through intensity gradients of shadowgraphy, schlieren technique, and interferometry shown in Figure 3.

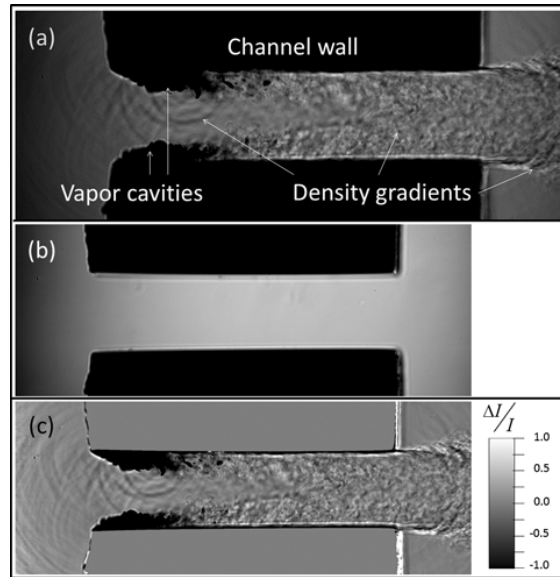


Figure 3: Shadowgraph-like (a) instantaneous image of the channel flow, (b) background image and (c) normalized intensity image [18]

Chen et al. [19] also had a closed loop of water with an inverted converging-diverging nozzle for cavitation studies. The study visualizes the evolution of the phase changing

behavior through high-speed video. They recorded the effect of Helmholtz cavity length on shedding period/frequency and length of cavitation. These and other previously reported works of phase changing flow through a channel lay a good foundation for the study of supercritical fluid flow through a nozzle undergoing a phase change.

1.3 Objectives

It can be seen that previous studies on condensation phenomenon of gaseous or supercritical fluids in a nozzle predominantly used a blow-down style test facilities. This restricts the amount of CO₂ which can be passed through a nozzle and requires less components in the facility. A closed loop system provides longer experimental run times that enable transient and steady analysis of nucleation behavior. The transient behavior of nucleation provides a time frame to examine the instability and development of phase change. Ushifusa et. al and Okamoto et al. investigated high speed optical diagnostics on supercritical carbon dioxide. These optical setups are inspiring as the area of interest is of similar scale to that of the studied nozzle in this thesis [20], [21]. Due to a sensitivity of carbon dioxide properties near the critical point, experiments are challenging to perform while maintaining the overall accuracy, especially in closed loop systems. The current work is an attempt to study the sCO₂ condensation in a closed-loop flow through a converging diverging nozzle that enables, unlike in open loop systems, longer experimental times under steady operating conditions. Previous numerical studies proved from computation that the nucleation effects are not significant to the turbomachinery components [13]. However, if the two-phase flow effects are to be enlarged, from a safety point of view, it is urgent to understand the overall fluid dynamics and flow environment inside the compressor. The current work also investigates the effect of inlet conditions and

flow dynamics on nucleation behavior through high-speed direct shadowgraphy. Figure 4 highlights a region of interest in a carbon dioxide T-s diagram with compressor inlet and throat conditions, indicated red and blue respectively. Based on these data points, several run cases will be formulated to visualize the nucleation effect near the critical point.

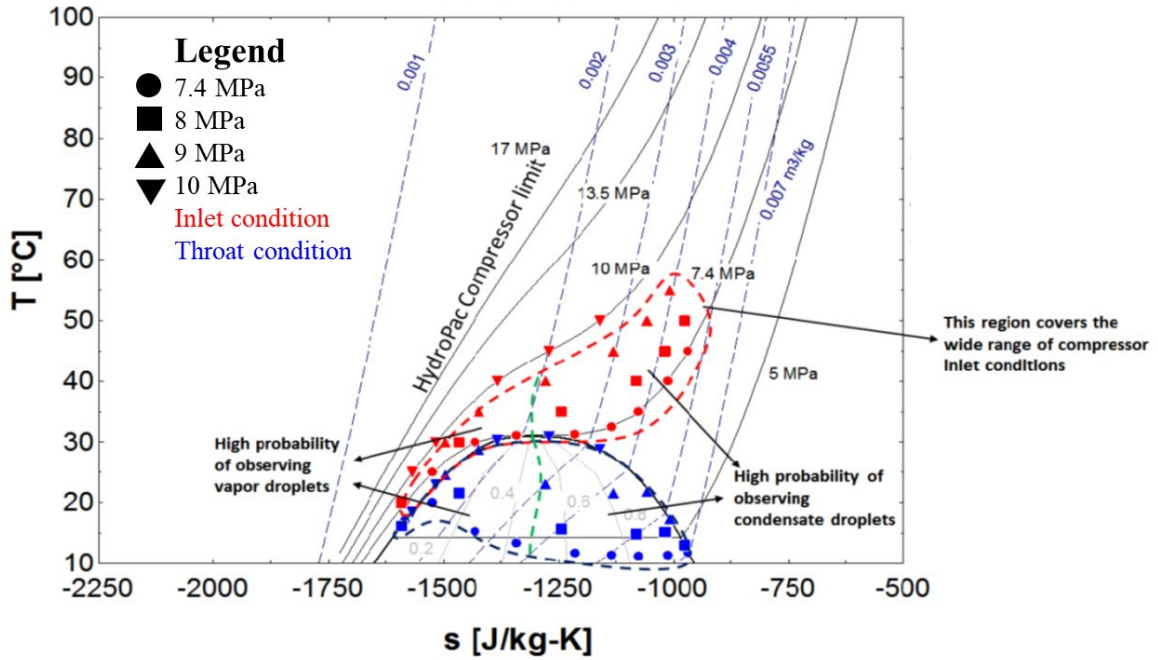


Figure 4: Compressor inlet and converging point conditions

CHAPTER 2. EXPERIMENTAL FACILITY AND SYSTEM

To study the condensation behavior, precise control of temperature, pressure, and flowrate before the test section is required to obtain a desirable flow condition within the test section. Thus, the flow requires constant controllable heating and cooling units, and a steady system for generating flow. To control these parameters, various components were connected in series found in Figure 5 and Figure 6 to meet the test conditions. In this chapter, each component of the experimental facility is discussed. Flow visualization is also discussed in the final section of the chapter.

2.1 Flow control equipment

2.1.1 Hydropac CO₂ compressor

To compress the CO₂ to a higher pressure, a Hydropac Inc (C02.4-40-2050LX/SSCO2) is used. The compressor is a single stage positive displacement type that can have outlet pressures of up to 16.5 MPa. The compressor requires a water-cooling unit for the outlet of hot CO₂ and piston-cylinder for cooling hydraulic Hydropac. A nominal capacity of flowrate capacity of the compressor is 120 scfm at -10 °C with 2.24 MPa suction pressure. To gain a desired flowrate and pressure, an input voltage signal is fed to the compressor. The voltage can be controlled by a Labview Data Acquisition program shown in Appendix H.

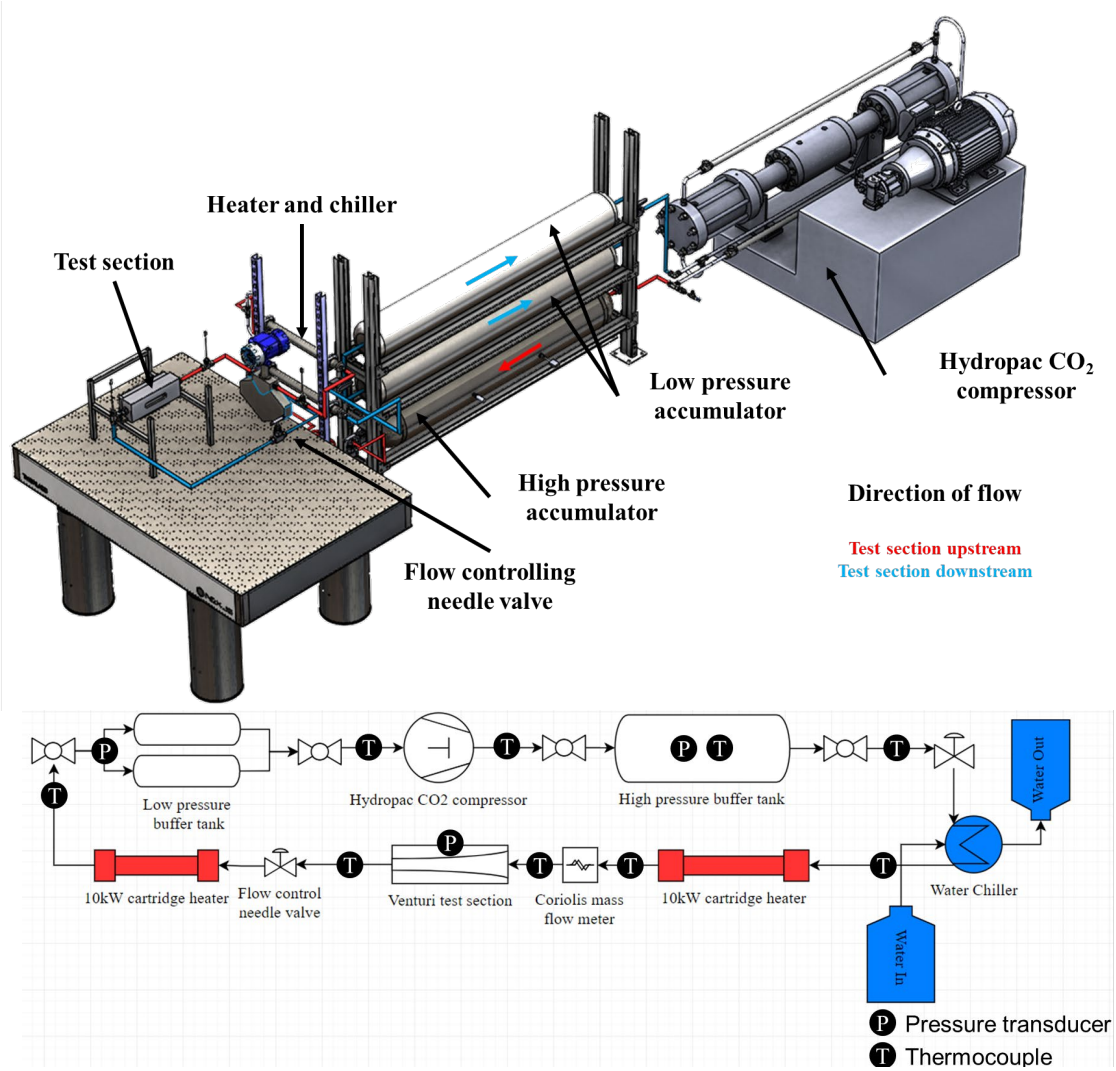


Figure 5: (top) 3D model of experimental facility and (bottom) 2D schematics of experimental facility with flow direction

2.1.2 High/low pressure accumulator

Because the compressor is a single stage positive displacement compressor, it is inherent to produce a pressure fluctuations in the overall system. To mitigate the pressure fluctuation, the system volume can be increased. High and low pressure accumulators (HP and LP) are attached upstream and downstream of the compressor respectively. HP accumulator is a Stainless Steel 316 tank with insulated heating jackets wrapped around the tank. In case the outlet temperature of CO₂ from the compressor is much lower than the

prescribed test condition, preheating the tank would reduce the heat load on the flow before entering the test section. The volume of the HP accumulator is 0.123 m^3 and is ASME stamped for pressure ratings up to 20.6 MPa. The LP accumulators are two 0.056 m^3 carbon steel tanks from Accumulators Inc. The choice of carbon steel as the material presents a concern of corrosion. However, the flow through the upstream of the tank is gaseous and is room temperature, and thus corrosion on carbon steel should be insignificant.

2.1.3 Heating/cooling components

In addition to the previously mentioned heating jackets wrapped around the HP accumulator, two 10 kW Tempco cartridge heaters are used to heat the flow. These cartridge heaters are installed in a heater assembly shown in Appendix F so that flow is heated while passing through the assembly. The heater is thermally anchored to the walls of the assembly by a high temperature thermal paste. One heater is connected before the test section to control the temperature of the inlet flow of the test section. The other heater is connected at the downstream of the test section to control the temperature entering the compressor. A counterflow coiled copper tube-in-tube heat exchanger is used as a chiller for the flow loop. It has a cooling capacity of 5 kW when supplied with water at a flow rate of 0.037 m^3 per minute at 10°C . The chiller and heater units are connected in series after the HP accumulator. The heater is connected after the chiller to make use of an active temperature feedback, which is not available in chiller.

2.1.4 Flow rate controlling needle valve

To control the mass flow through the test section, a needle valve is placed before the chiller. The needle valve is a Swagelok Female $1/2''$ NPT connection (SS-8GUF8). Mass

flow rate and pressure upstream of the test section is controlled with this valve. A second flow-controlling valve (SS-5PDF8) is located at the downstream of the test section to control the downstream pressure of the test section. This allows precise control of the pressure at both test section inlet and outlet through the number of turns of both valve handles. The specific model was chosen based on the flow coefficient calculation more explained in Appendix G.

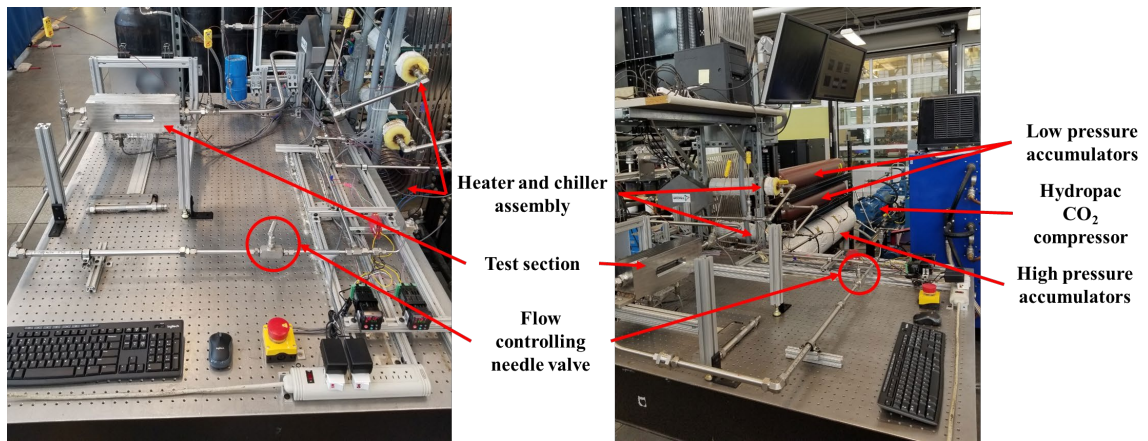


Figure 6: Actual experimental setup images with facility components

2.2 Test Section

The test section is composed of stainless steel 316 flanges assembled to form a rectangular converging-diverging channel (assembly and actual images presented in Appendix F). It was fabricated by Marine Technologies and was hydro-tested for its integrity up to 26 MPa. Two flanges and a body form the frame of test section. The body holds the other two flanges in place with 10-32 and 1/4"-20 hex nut screws. The bottom flange has ten pressure taps to measure the static pressure along the nozzle profile as shown in Figure 7 and Appendix J. The pressure tap locations are closer to each other near the throat to record higher resolution pressure fluctuations near the throat region.

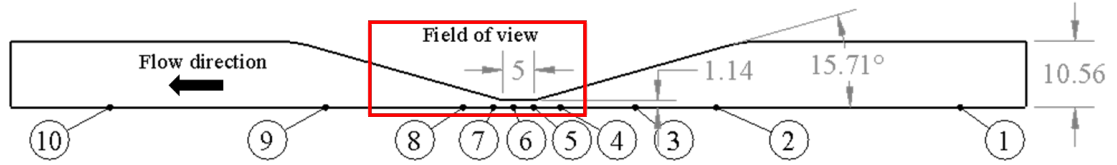


Figure 7: Flow profile geometry with pressure transducer locations

The back flange has a 3 mm slot to place a nozzle profile using a flat-head screw and dowel pins. The modularity of this design allows for changes to be easily made to the nozzle profile. Intrusive probes to measure the temperature inside the nozzle are avoided as they could significantly affect the condensation behavior of the fluid (especially due to the stagnation points). The test section has two sapphire glass windows (one on the body and the other on the back flange) for visualization and optical measurements. Sapphire glass is used instead of quartz for its high compressive strength and scratch resistance. Calculation for sapphire glass window thickness is shown in Appendix D. The nozzle profile is made out of a 3 mm thick 316 stainless steel sheet. The desired profile is three dimensionally modeled and milled using a CNC machine loaded with a CAM file. The currently used converging diverging nozzle profile shown in Figure 7 has an expansion rate of 2500 s^{-1} .

Though not covered in this thesis, the test section can also perform supercritical carbon dioxide erosion experiments by exposing different material samples to sCO_2 . A sample piece holder is cut out in an L-shape from the bottom flange so that a material sample such as aluminum or Inconel 625 sample pieces can be inserted. The change in mass of the piece from before to after the experiment indicates the corrosion rate and extent. These samples are precisely cut by EDM technologies. From several exposure of

supercritical carbon dioxide flow, it is seen that there is not a significant change in weights. This indicated that far more quantitative measurements such as skin friction coefficient measurements are required to bring a significant conclusion to the sCO₂ material degradation test.

Due to high pressure and glass wall surfaces, flanges required o-ring installation to prevent the metal surface from contacting and damaging the sapphire glass window. Before installation of o-ring, stainless steel shim stocks were placed between the flange and window wall, but the seal was not effective. Shim stocks were replaced with o-rings and showed huge improvement of leak-free environment, by having leakage rate of 0.014 MPa/hour when pressurized to the test conditions. To minimize the volume and maximize the surface area contact for a proper seal, 1 mm Viton chemically resistant o-rings were used on the nozzle face and bottom flange shown in Figure 8.

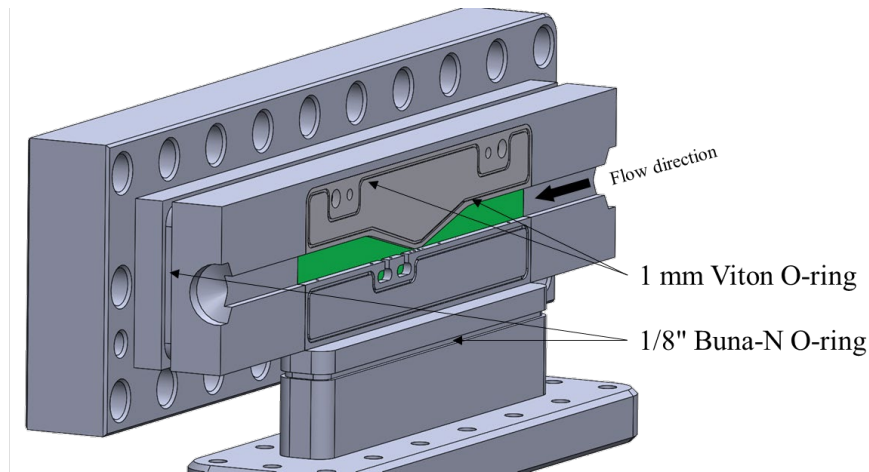


Figure 8: O-ring location on nozzle face and bottom flange face

For sealing between flanges and the body, 1/8" Buna-N 70A o-rings were placed with a small amount of vacuum grease to allow flanges to be leak-tight. To further enhance the

sealing, x-profile o-rings were used instead of round cross-section. X-profile o-rings provide two points of contact instead of one, giving a further leak-tight environment.

2.3 Instrumentation

Temperature and pressure measurements were required at each inlet or outlet of the experimental facility. Because the supercritical CO₂ flow and fluid properties are very sensitive to temperature, K-type thermocouples from Omega Engineering are calibrated with Isotemp 2150, an accurate hot water bath from Fischer Scientific. To measure the pressure of the accumulators, Omega-dyne PX309-3KGSV are used. These pressure transducers were calibrated using a dead-weight sensor (Amthor 452). The Model name calibration verified the sensitivity of the pressure transducer given input voltage supply of 24 V. Pressure measurements at the test section were taken by two different sets of equipment. To record high-speed pressure measurements, Kulite ETM-375CO pressure transducers with a natural frequency greater than 400 kHz were used. For more precise pressure measurement, Meriam M1500 pressure transducers were used, collecting 14 samples per second with an accuracy of 0.03% of full scale. A TCM 3100 Coriolis flow meter from Tricor was used for mass flow measurement. The accuracy of the mass flow meter is 1% of the flowrate. This gives the maximum error of the flow meter to be 0.0086 kg/s. Table 1 summarizes the accuracy of these instrument used in the experimental facility.

Table 1: Accuracy of instrumentation used in the experimental facility

Instrument	Model Name	Accuracy	
Thermocouple	CASS-18E-12	2.2 °C	0.75%
Pressure Transducer	Meriam M1500-G3000	0.75 psi	0.03%
	Kulite ETM 375-CO	2 psi	0.01%
	Omegadyne PX309-3KGSV	7.5 psi	0.25%
Flow meter	Tricor TCM 3100	8.6 g/s	1%
Water bath	Fischer Scientific Isotemp 2150	0.02 °C	0.03%
Pressure calibration kit	Amthor 452 Pressure tester		

2.4 Safety Features

Phase transition from a supercritical state to a two-phase state required high-pressure ratings for the loop components. Because the experiment is rated at high pressure, safe design of the loop was the first priority. In the case of high pressure burst or leak, a safety mechanism of stopping flow was necessary. To build a pressure-rated loop, compression fittings from Swagelok were used as the max pressure ratings at temperature of 25 °C is 53 MPa. Due to the corrosive nature of CO₂, all tube materials were chosen as stainless steel 316. To calculate the minimum tube wall thickness, the ASME B31.1-2016 pressure piping code was used. Based on the extreme test conditions, which are 10 MPa and 50 °C, the following properties were obtained in Reference [22] Section 104.1.2. Based on the ASME B31.1-2106 code, the minimum thickness was 0.025". The calculation table is shown in Appendix C. With manufacturing tolerance and an additional safety factor of 2.5, the tube thickness was chosen at 0.065".

In case of flow blockage or leakage from the compressor, the heaters and the compressor signal lines are connected to an emergency stop. This ensures that the power

for the heaters are turned off and the compression work is set to zero in the case of an emergency scenario.

2.5 High speed direct shadowgraphy

The nucleation process near the throat of the nozzle was observed using a direct back-lit, high frame-rate shadowgraphy. The setup is presented in Figure 9. Previous works have used other techniques such as basic interferometry, shearing interferometry, and Mie scattering to measure the density gradient of the flow field quantitatively. However, these setups require precise calibration and many optical components. For the sake of simplicity and purpose of observing the qualitative flow behavior, direct shadowgraphy is chosen for the current work with a light source and a camera. The light-source was a 250 Watt Lowel Pro light mounted on an optical rail.

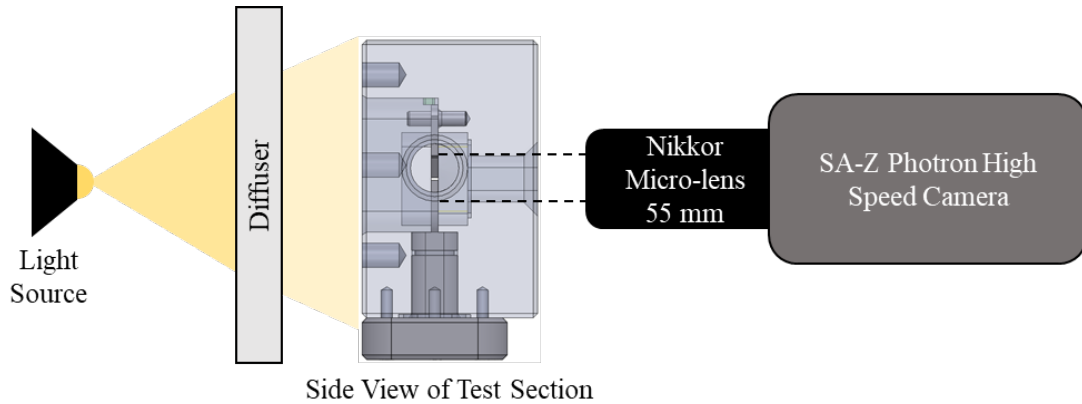


Figure 9: Schematic of the high-speed direct shadowgraphy setup (test section flow is into the page)

Given the anticipated condensation time-scales [$O(0.1 \text{ ms})$], a Photron SA-Z high-speed camera, capable of frame-rates from 60 fps to 20,000 fps at 1M pixels was used for shadowgraphy. For the purpose of resolving the high-speed phenomenon of nucleation, the

imaging was done at a reduced resolution of 1024×512 pixels and a frame rate of 40,000 Hz. The camera is focused on the test section so that the back-lit carbon dioxide flow can be directly captured without a loss of intensity that occurs when projected onto a plane. It must be noted that the shadowgraphy is a line-of-sight averaged technique, and depicts the flow phase transition behavior across the thickness of the test section. The field of view of the shadowgraph where the nucleation behavior was observed is indicated in Figure 7. High speed direct shadowgraphy is performed under three different flow phase transition: supercritical flow, condensing flow, and cavitating flow, which are found in Figure 10. Different flows are recorded to take a sense of the image intensity signals for image processing.

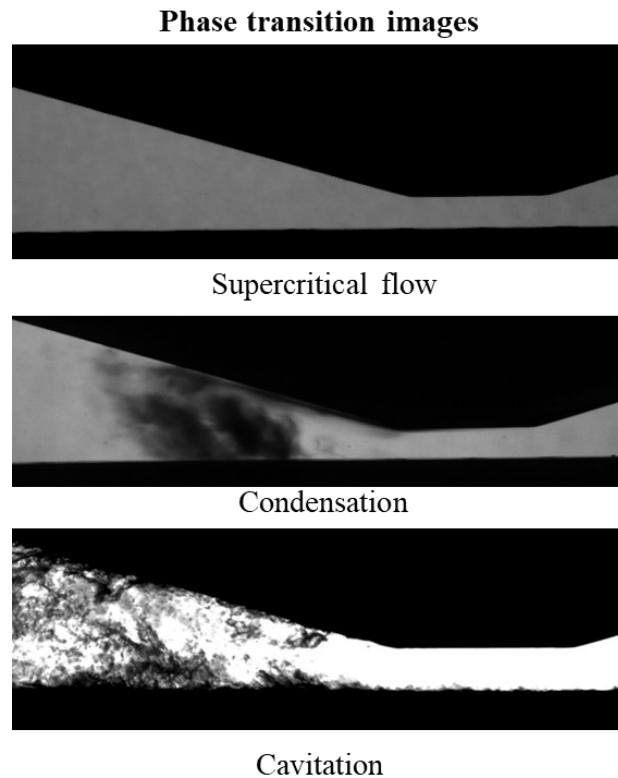


Figure 10: Phase transition images of different flows

CHAPTER 3. EXPERIMENTAL PROCEDURE AND OPERATION

Many of the experimental facilities and test components are isolated and remain pressurized while the experiment is not conducted. There is a potential of o-ring failure, fitting failure, and tube burst when the compressor drives the CO₂ while any of the valves are closed. It is critical that these valves are open and test components are operated at a safe level for the best performance. Figure 11 indicates locations of all valves in the experimental facility and the flow direction. This chapter presents a safe and efficient manner of conducting the experiment and a guidance to preparation and closure of an experiment.

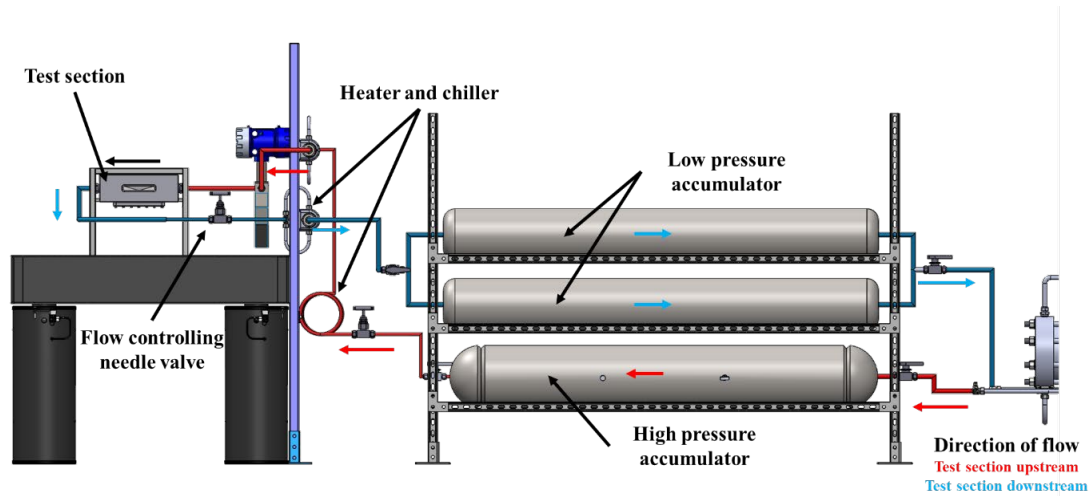


Figure 11: Side view of experimental facility with flow direction

3.1 Pre-experimental setup

Initial filling of the LP and HP accumulators is done by commercially purchased CO₂ gas tanks with an initial pressure of 800 psi. Once the pressure gradient between the

commercial gas tanks and the accumulator is close to zero, no flow is driven inside the tank. To satisfy a closed-loop condition, both HP and LP accumulators are charged up to 5.51 MPa. The tanks are isolated from the loop and the compressor is turned on to drive the CO₂ from the LP accumulator to high-pressure accumulator. This process is done until the HP accumulator is at 7.58 MPa and LP tank at 3.44 MPa at a room temperature. Then the heat jackets on the HP accumulator are turned on to set the fluid temperature to be 50 °C. The heating jacket power input is controlled via a pulse width modulation with 10 millisecond duty cycle so that the desired fluid temperature is reached slowly. This process should take about a day to settle the temperature and pressure of both tanks.

3.2 Experimental procedure

Before turning on the compressor, chilled water supply should be turned on and confirmed that the water is flowing through the cooling jackets of the compressor by slightly opening the water exhaust line. The compressor motor is turned on to begin the experiment. All the ball valves that isolate the two types of accumulators are opened so that the CO₂ can flow through the test section and compressor. This is a crucial step so that the compressor does not compress dry air or pushes the CO₂ out to a closed valve. Failure to follow this step will create large pressure build up near the tubing assembly near the compressor that poses a risk of tube burst or fitting failure. All the control valves should be initially fully open and gradually closed slowly to reach the targeting test section pressure and mass flow rate.

Once a constant flow rate of CO₂ is driven to the test section the heater assembly should be turned on to keep the flow temperature steady. The cartridge heater assembly is

controlled using a heater controller by Watlow EZ-Zone controller. This controller offers manual and automatic control using a feedback temperature from a K-type thermocouple. The set point temperature can be designated either physically on the controller or on the computer through a software provided by Watlow.

Controlling three parameters (pressure, temperature, and flow rate) is challenging because of their dependence on one another. Once the pressure and temperature are stabilized in running the experiment, the mass flow controlling valve should be slowly closed to reach the desired mass flow from the Coriolis flow meter. Then the pressure of the downstream tank should be slowly adjusted. The temperature should be controlled last so that the flow is slowly heated while maintaining the rest of the conditions. In the case of over pressurization, the flow controlling valve should be slowly opened so that the pressure is lowered. It is essential that these valves be controlled carefully as the pressure and flow rate are very sensitive to the turns at these test conditions.

Before the experiment, a sheet of paper is taped onto the glass window inside the test section so that the camera is focused onto the back wall of the optical window. sight. Once condensation is visible after constant CO₂ is driven through the test section, direct shadowgraphy is performed using the Photron SA-Z camera. The light source is turned on and the light is directed onto a diffuser sheet before reaching the test section. The high-speed camera is set to 40,000 frames/second with the smallest aperture so that the focused image of the condensation can be distinguished based on the light intensity. Because supercritical CO₂ is a clear fluid, it permits light through the test section and is seen as white by the camera, while the condensation, which takes the form of a white cloud, will be seen dark due to an absorption of light rays. The camera is synchronized with the data acquisition so that once a trigger is given from the camera, the Labview DAQ begins to take pressure and temperature measurements of the loop based on the set frame rate.

3.3 Experiment closure procedure

This process is critical to perform so that the experimental setup is not left pressurized without an intention. To end the experiment, first all the heating units must be turned off. It is crucial that the heaters are turned off first so that the tubes are not heated without the flow. All of the flow controlling valves are fully opened. Then, the mass flow controlling valve and the ball valve at the outlet of the HP accumulator are fully closed so that no flow is directed toward the test section. This will cause a pressure decrease in the test section and LP accumulator. Once, the pressure inside the lower pressure accumulator is close to 1.72 MPa, the compression work is turned off and the valves for inlet of the LP accumulator are closed. In addition, the compressor is isolated so that no back flow is directed toward the compressor by shutting off the inlet of the HP accumulator and outlet of the LP accumulator. Now that the test section is isolated, the test section can be vented for replacement of o-rings or change of nozzle profile. Any irregularities in the test loop should be inspected by monitoring the temperature and pressure of the test loop. The last step is to turn off the compressor motor and the power source from the electrical panel.

CHAPTER 4. THEORETICAL CALCULATION AND EXPERIMENTAL RESULTS

Pressure and optical diagnostics data are recorded simultaneous for each of condition shown in Table 2. Figure 12 shows a T-s diagram of the test conditions. Among these conditions, Run #3 did not meet the criteria of observing a phase change. However, conditions of run #1 from Table 2 led to non-equilibrium condensation of carbon dioxide. Non-equilibrium phase change is a phase change driven by an external factor (other than a thermal gradient), in this experiment, a contraction in cross-sectional area. This chapter discusses the theoretical calculation of CO₂ flow using the homogeneous equilibrium model and compares these calculations to the experimental data. This chapter also analyzes high-speed shadowgraphy results of supercritical carbon dioxide nozzle flow near the critical point.

Table 2: Experimental conditions at the inlet of the test section

Run #	Pressure (MPa)	Temperature (°C)	Mass flow rate (kg/s)	Divergence Angle (deg)	Phase Change
1	7.4	31.4	0.05-0.055	15	Present
2	7.5	32	0.05 - 0.065	15	Present
3	7.8	33	0.05 - 0.065	15	Not Present

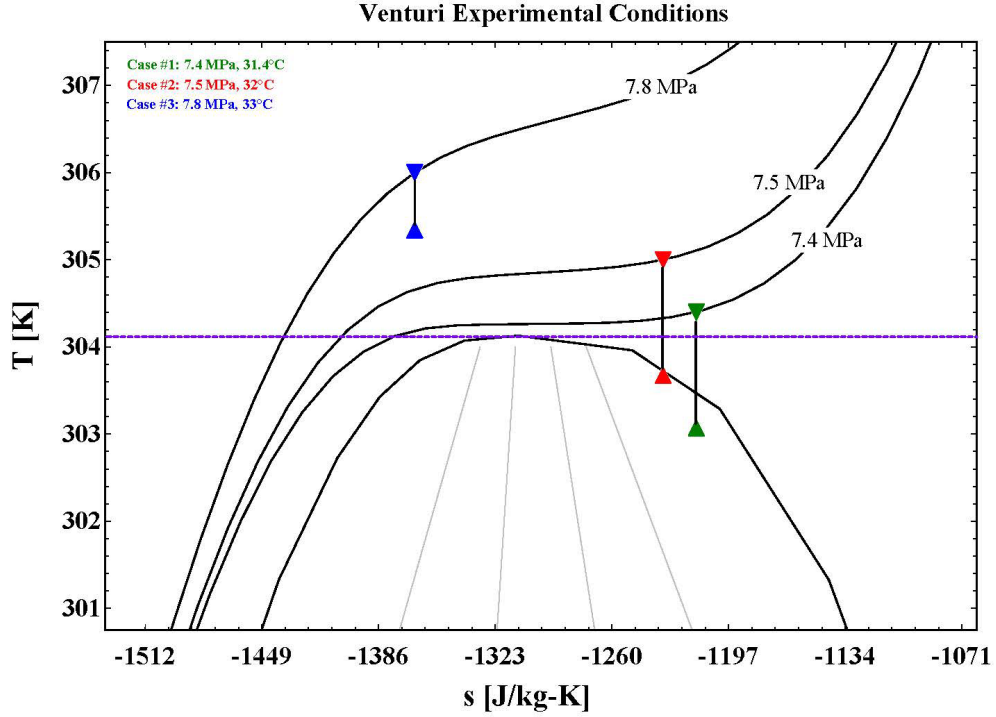


Figure 12: Experimental test conditions on T-s diagram

4.1 Theoretical model calculation and comparison

Based on the findings of Jarrahbashi et al, the flow profile with the geometry presented in this thesis observed a non-equilibrium condensation phenomenon near the throat. This is because the residence time at the throat is much greater than the nucleation time at flow conditions of near critical point [15]. Residence time is a time scale that the nucleation resides on a location of incipience. The nucleation time is determined by nucleation rate and volume of the nucleation shown in Equation 1 [8],

$$t_{residence} = \frac{l}{V_{avg}}, \quad t_{nucleation} = \frac{1}{J_{max} \mathbb{V}} \quad (1)$$

where $t_{residence}$ is the residence time, l is the characteristic length, V_{avg} is the average velocity of the flow, $t_{nucleation}$ is the time to form a nucleation, \mathbb{V} is the volume of the nucleating particle, and J_{max} is the maximum nucleation rate based on the flow condition. To verify the non-equilibrium condensation, one-dimensional calculation was performed at the nozzle with runs specified on Table 2. Using REFPROP and MATLAB, a homogeneous equilibrium model of CO₂ flow is developed for the specific geometry. The homogeneous equilibrium model is used to calculate the thermophysical properties of CO₂ at a given flow condition. The model relies on following assumptions: 1. the flow is in mechanical and thermal equilibrium. 2. The flow does not lose heat along the nozzle and is isentropic. Mechanical and thermal equilibrium indicate that both the phases of carbon dioxide during condensation in the nozzle flow are travelling at the same velocity and have the same temperature and pressure at any location. The flow profile was divided into a distinct number of segments, and within each segment, properties were calculated based on the previous flow conditions. The equations for conservation of mass and energy balance are shown in Equation 2 and 3 respectively,

$$\frac{d}{dt} \int_{cv} \rho d\mathbb{V} + \int_{cs} \rho (\vec{V} \cdot \vec{n}) dA \rightarrow (\rho VA)_{i+1} - (\rho VA)_i = \dot{m}_{i+1} - \dot{m}_i = 0 \quad (2)$$

$$\frac{dQ}{dt} - \frac{dW}{dt} = \frac{d}{dt} \int_{cv} \left(u + \frac{V^2}{2} + gy \right) \rho d\mathbb{V} + \int_{cs} \left(u + \frac{V^2}{2} + gy \right) \rho (\vec{V} \cdot \vec{n}) dA = 0 \quad (3)$$

where cv is a control volume, cs is the control surface, ρ is fluid density, A is the cross-sectional area, \dot{m}_i is the mass flow going through the cross-section at the i^{th} segment, h is fluid enthalpy, g is the gravitational constant, and y is the height of control volume.

From the inlet temperature and pressure, other relevant properties such as entropy (s_0), enthalpy, and density can be calculated and used as boundary conditions to solve the equations. Based on the flow velocity, friction and acceleration pressure drop for each segment were compensated for the next control surface segment pressure using Equation 4. Each segment calculates control surface quality to check whether the flow requires two-phase properties calculation. When the flow passes through a converging section of the nozzle leading to two-phase properties, Equation 5 and 6 are respectively used to calculate mixture density and viscosity [23].

$$\frac{dP_{friction_i}}{dx} = \left(\frac{f_i \cdot G_i^2}{2 \cdot \rho_i \cdot D_{h_i}} \right), \quad \frac{dP_{acc_i}}{dx} = \frac{G_{i+1}^2}{\rho_{i+1}} - \frac{G_i^2}{\rho_i} \quad (4)$$

$$\rho_m = x \cdot \rho_l + (1 - x) \cdot \rho_g \quad (5)$$

$$\nu_m = x \cdot \nu_l + (1 - x) \cdot \nu_g \quad (6)$$

Figure 14 show a how fluid properties and behavior change along the nozzle profile in a non-dimensional form. Using the pressure calculations obtained from Figure 14, theoretical calculations were compared to the experimental pressure measurements in Figure 15.

Experimental measurements were taken at the mid-plane of the flow profile. A computational study by Jarrahbashi et al. for a similar nozzle profile yielded different condensation phenomena when evaluated along the side walls of the flow profile (window glass plane). An OpenFOAM simulation for a transient supercritical carbon dioxide flow through the current nozzle profile observed that the nucleation rate along the nozzle profile was greater on the side-walls than in the middle plane. When the effects of surface tension

were considered, more nucleation occurred along the lateral walls of the profile rather than the bulk of flow shown in Figure 13 [15].

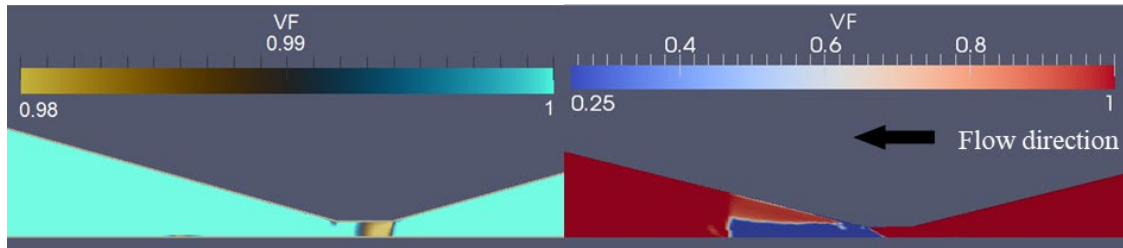


Figure 13: Comparison of void fractions (left) on central plane and (right) on the wall plane of the flow profile [15]

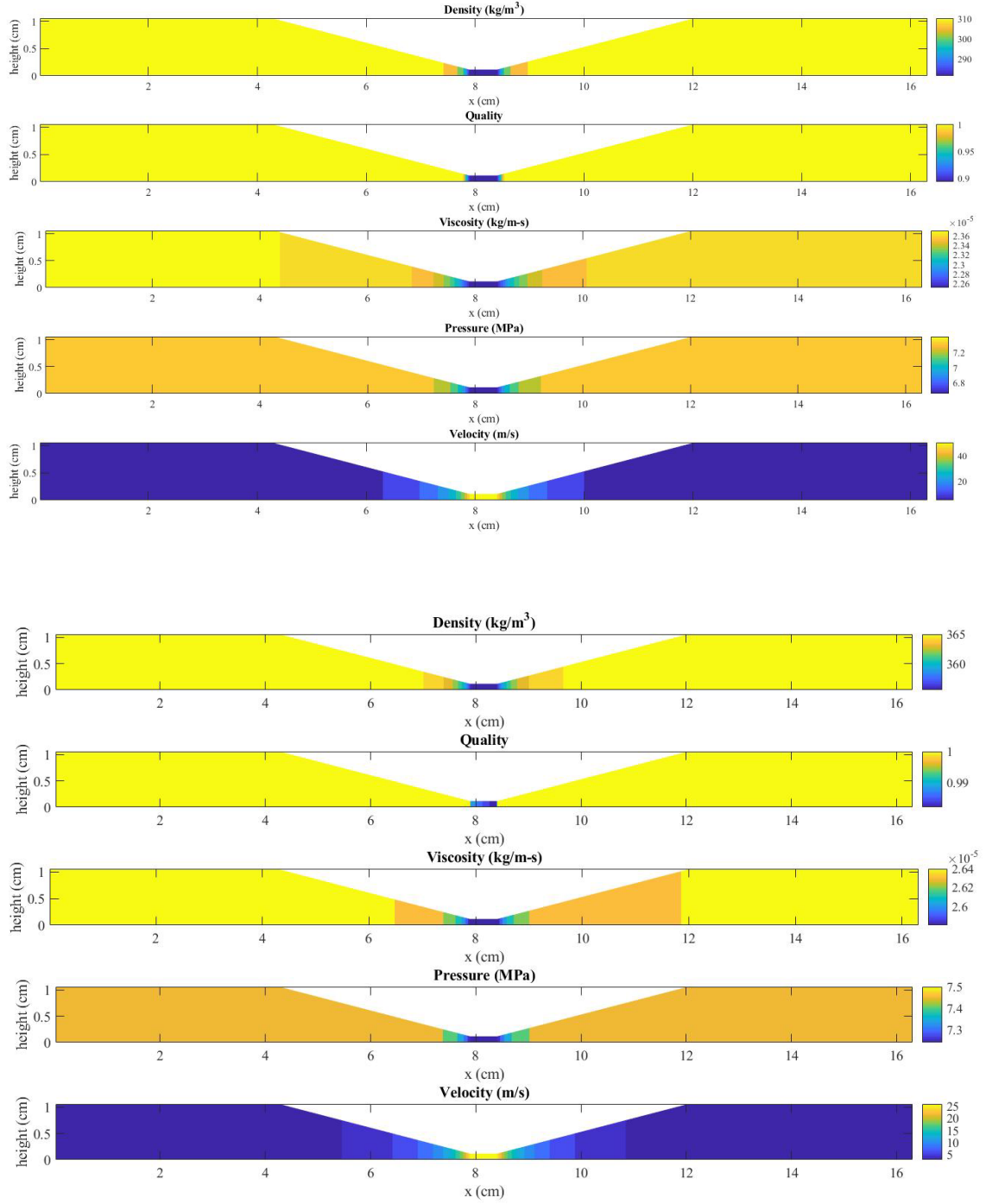


Figure 14: HEM results on flow profile for (top) 7.4 MPa 31.4 °C and (bottom) 7.5 MPa 32 °C

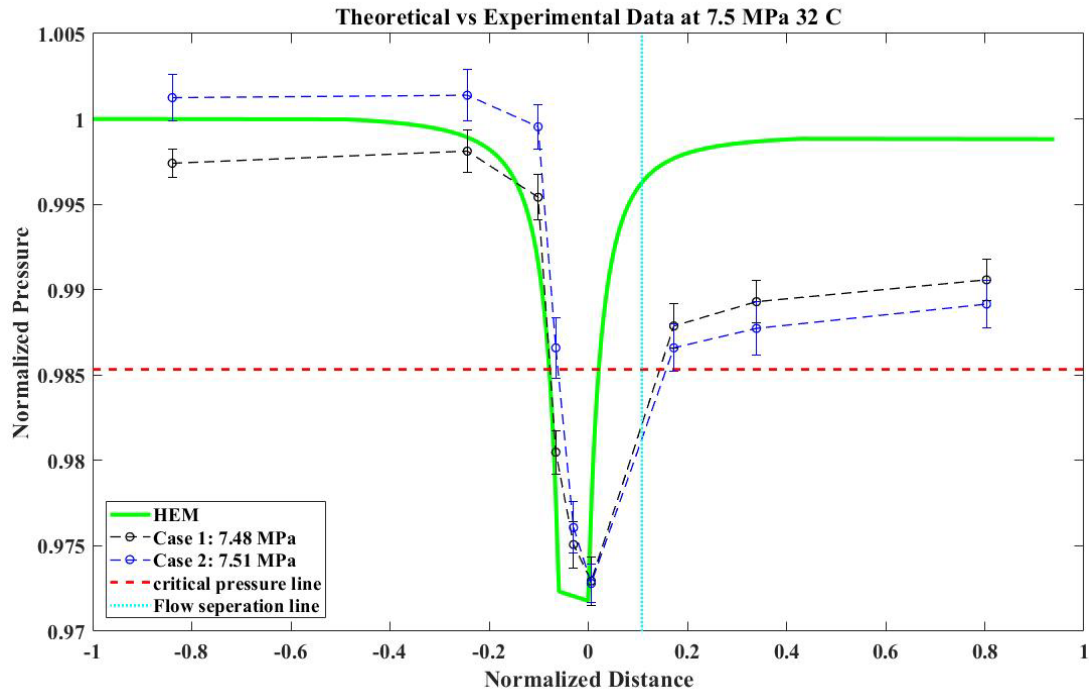
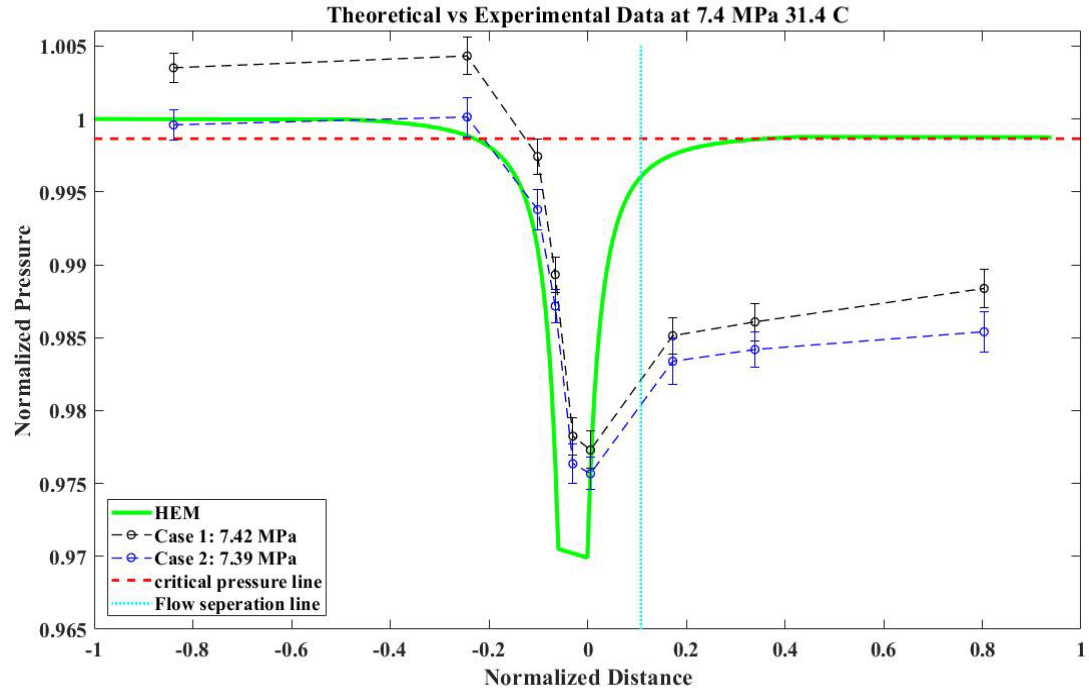


Figure 15: Comparison between homogeneous equilibrium model and experimental data for (top) run #1 (bottom) run #2 of test conditions

While the analytical model agrees well with the flow on the converging section and the throat (favorable pressure gradient), the agreement is poor in the diverging section where condensation occurs, with the experimental measurements showing lower pressure than the predicted values shown in Figure 14. This can be attributed to the separation of flow in the diverging section and the recirculation zone; the pressure could not be recovered as predicted by the analytical model. It can be predicted that the location where the separation occurs is within 7 mm away from the throat. Jarrahbashi et al. also showed the region of recirculation zone that is 9.1 mm away from the throat, which can be found from Figure 16.

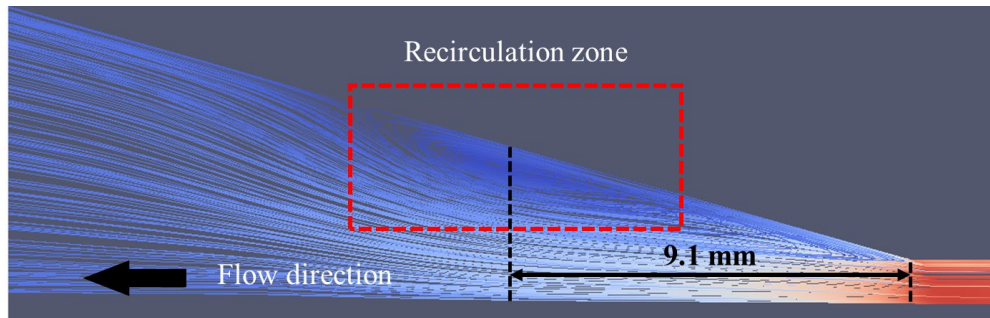


Figure 16: Indication of recirculation zone in velocity field vector along the flow profile [15]

This disagreement between the experimental and analytical results will be improved with the manipulation of the geometry and surface properties of the test section such as a decreasing diverging angle to eliminate the recirculation zone, as was shown computationally by Jarrahbashi et al [15].

4.2 Visualization of non-equilibrium condensation

Based on the pressure and temperature of the flow near the throat, the length of the condensation behavior can be changed dramatically. Referring back to Figure 12, the first run shows the throat location is inside the two-phase dome for CO₂, compared to the second run, which lies on the saturation curve line. Figure 17 is a captured series of images of non-equilibrium condensation development when first run of the experimental conditions were obtained in the test section.

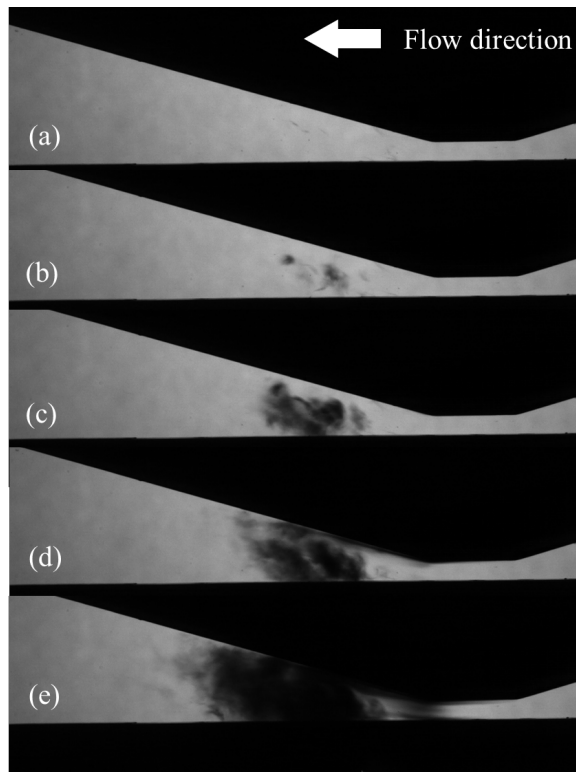


Figure 17: Development of non-equilibrium condensation as it reaches

In Figure 17(b), the phase change point occurs 8.83 mm downstream of the throat. As the instability of the flow increases entering into the metastable region for CO₂, the local quality of the flow decreases and the phase change starts to happen closer to the inlet of the throat. As the liquid volume fraction increases on the incipience of the nucleation spot, the phase change phenomena grows along the flow profile. Both Lettieri et. al and

Jarrahbashi et. al point out that the condensation front shifts based on the inlet conditions of the nozzle [8, 15]. In Figure 17(e), the phase change phenomenon is not focused near the throat and is represented as a blob in the image, an indication that the phase change location is closed to the center plane of the flow profile than the wall plane. This finding coincides with the finding of void fraction difference between wall plane and center plane from Jarrahbashi et al. [15]

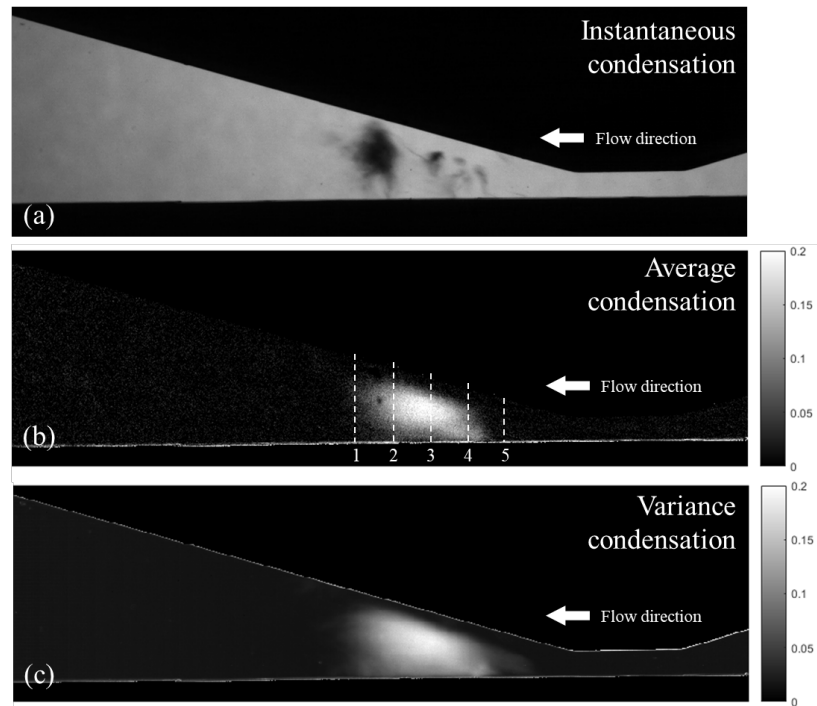


Figure 18: a) Instantaneous raw shadowgraph, and (b) average, and (c) variance of β . Lines 1-5 in (b) indicate locations where ϕ_β was computed

Figure 18(a) shows an example raw shadowgraph image that clearly shows the instantaneous condensation behavior captured downstream of the throat. The highly unsteady nature of the condensation occurrence was captured over a period of half a second (limited by the camera memory) arising from the proximity of the flow conditions to the critical point and turbulent nature of the flow. The condensation appears in the form of

white cloud near the throat region, which should otherwise not be present in a purely supercritical phase. Unlike flow regimes shown by Cognata et al. [24] where bubbles are expected in the microscale due to high mass flux, a mist flow regime is shown in the instantaneous condensation image. In this flow regime, the bubbles are too small for any optical analysis presented in this thesis. X-rays or Mie scattering could be used to resolve the bubbles, but would also have to be high enough resolution to view the entire phenomenon to be significant. From these raw images, a relative void fraction was calculated by adjusting the intensity with a reference image (taken before the experiment) that showed no condensation in the CO₂ flow, normalizing the image, and inverting it to get the relative volume fraction (β) of the condensed phase. Figure XX shows the image processing steps of how to achieve a relative void fraction image.

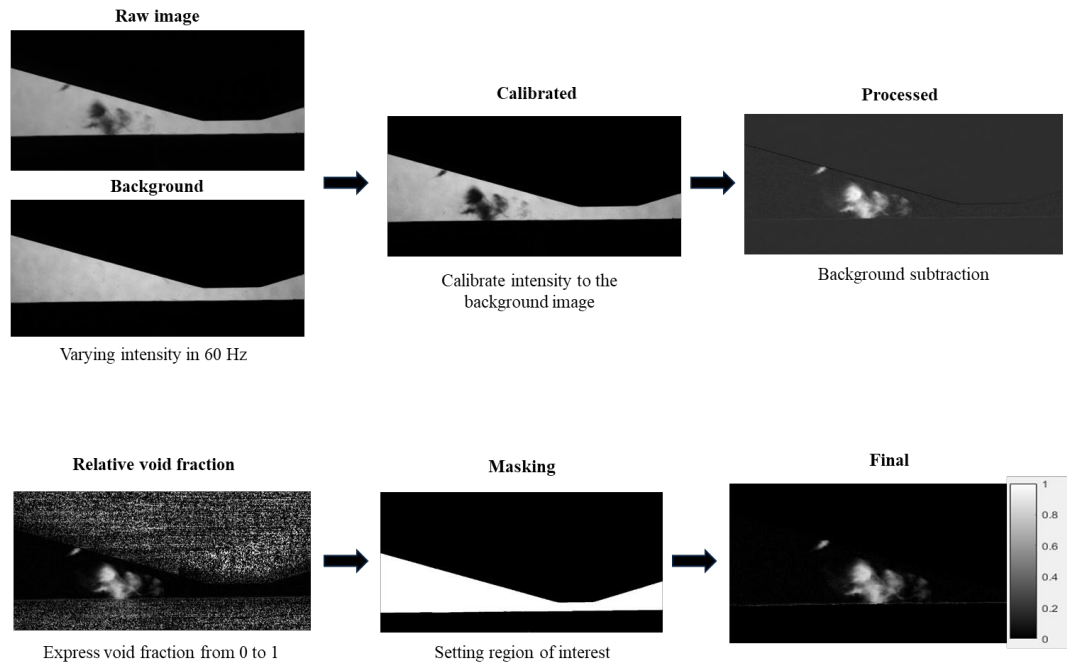


Figure 19: Image processing steps for relative void fractions

Further, the condensation in the test section periodically oscillates resulting from the slow variations of the experiment conditions [$O(10\text{ s})$]. However, owing to the very fast evolution of the nucleation (calculated from the time scale analysis of non-equilibrium condensation) and condensation behavior in the current case [$O(0.1\text{ ms})$], a finite time interval [$O(80\text{ ms})$] where the condensation behavior was statistically stationary can be identified. This interval is set as the quasi-stationary region and considered only a part of the signal to compute our turbulence and void fraction statistics. Figure 18(b) and (c) show this time-averaged distribution of the condensation and its corresponding variance, with intensity representative of the volume fraction of the condensed CO_2 . The condensation can be seen to be localized immediately downstream of the throat as the flow separates. This condensation disappears as the condensed CO_2 re-evaporates farther downstream of the throat.

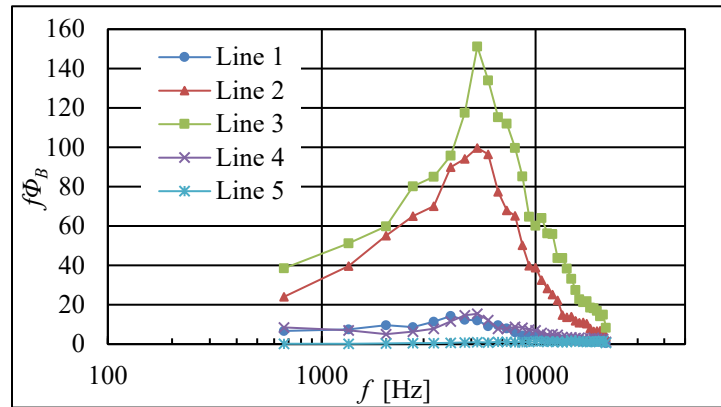


Figure 20: Power spectral density, ϕ_β , over five different locations marked in Figure 18(b)

While the nucleation and condensation phenomenon was found to be highly unsteady due to instability in the metastable region, a distinct intermittency and shedding of condensed

‘clouds’ were observed. To investigate this further, average ‘volume’ of condensed CO₂ (represented as $\tilde{\beta}$,

$$\tilde{\beta} = \int \beta dy / H \quad (7)$$

where H is the channel height at the location and y is normal distance to the bottom wall) at selected cross section areas (marked as dashed lines in Figure 18(b)) were extracted from the time series. Figure 20 plots the pre-multiplied power spectra $\Phi_{\tilde{\beta}}$ of $\tilde{\beta}$, that clearly identifies a dominant shedding peak at $f_s \approx 5343 \text{ Hz}$ at all corresponding cross section areas. Given that the shutter speed was a 42,748 frames per second, the dominant frequency of 5343 Hz results in 8 frames of the entire video. The high speed video was replayed to observe every 8th frames. Figure 21 shows a few example frames of void fraction with a delay corresponding to $\tau = 1/f_s$. The periodicity and the shedding of the condensation clouds is evident and repeatable, as can be seen in the ‘strobed’ images. This indicates that the condensation behavior at the inlet condition of 7.5 MPa with 32 °C of the studied nozzle profile is periodic and happens every 0.187 milliseconds at the downstream of the throat. The frequency of this condensation behavior is a function of a separation point. The separation point location can be changed based on the flow conditions and geometry of the flow profile. A conclusion can be reached that the condensation behavior at a specific flow condition and nozzle geometry is statistically stationary.

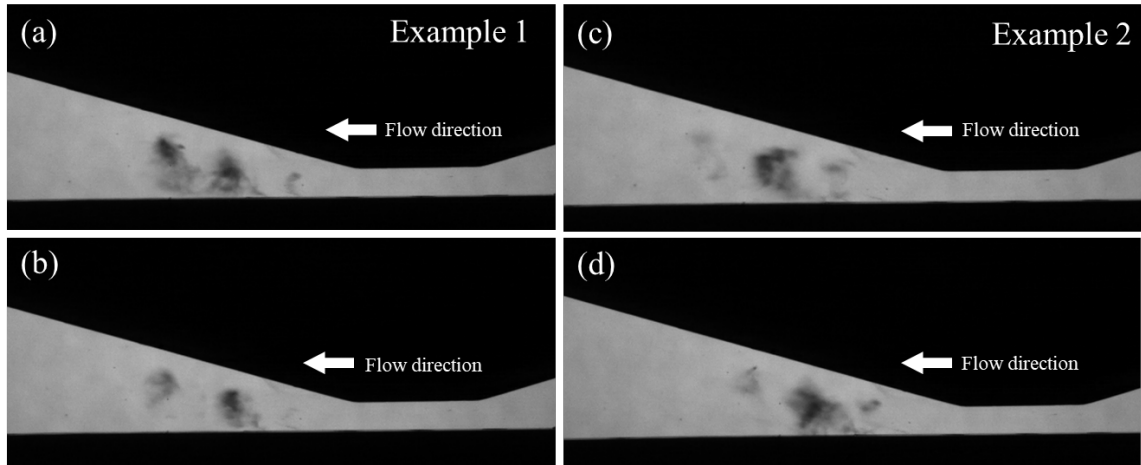


Figure 21: Two example sets of images [(a) and (b), (c) and (d)] for successive frames of condensation separated by $1/f_s$

CHAPTER 5. CONCLUSION AND FUTURE WORK

5.1 Conclusion

Motivation in examining supercritical carbon dioxide flow phase transition led to a CO₂ flow through a converging-diverging nozzle experiment in a closed-loop facility. Key components to control three parameters of the flow (temperature, pressure, and flow rate) were added on the experimental setup to drive a supercritical flow through a test section with a fabricated nozzle profile. Inlet and outlet flow conditions and experimental measurements of pressure profiles along the nozzle indicated a presence of flow separation. This led to a deviation when compared with a theoretical calculation using the homogeneous equilibrium model at the downstream of the nozzle throat. The location of flow separation was estimated by a numerical study of similar geometry done by Jarrahbashi et. al [15]. Phase transition behavior is explained in term of hydrodynamics by using a high-speed direct shadowgraphy on the condensation behavior. Based on the studied geometry of the flow profile, a dominant shedding frequency of nucleation behavior was discovered through calculation of power spectral density analysis. The high-speed video was replayed at this frequency to verify a strobe image of phase change at the downstream of the throat. It can be concluded that the periodicity of the supercritical phase transition is based on the flow geometry and flow conditions that govern the location of the separation point.

5.2 Future work

5.2.1 Closed-loop facility and test section

Because the experiment was conducted on a closed-loop facility, the mass flow through the test section was comparatively small to other previous studies. A comparison between blowdown experiments and a closed-loop setup can be conducted to observe the transient effect on the nucleation behavior.

The pressure measurement in this test section was challenging due to a physical limitation in depth of the nozzle profile. Electrical discharge machining was done to make a 1/16" pressure tap along the bottom wall of the nozzle. A wider nozzle in depth should be used to ensure a two dimensional effect and the direct static wall pressure measurement for high frequency recording.

Currently, variation in geometry of nozzle design for a change in nucleation behavior is still ongoing. Referring to flow regimes of a diffuser design in [25], different angles of nozzle are being fabricated to note a change in nucleation behavior downstream of the throat shown below.

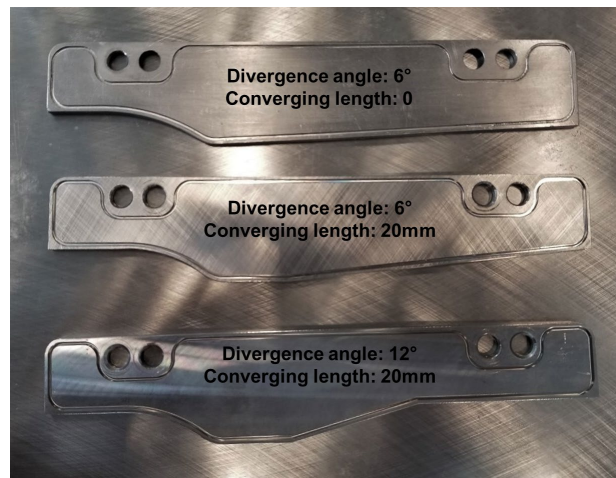


Figure 22: Nozzle geometry variations for different flow regime

5.2.2 Non-intrusive measurement using orthogonal optical access

In this scope of work, only high speed shadowgraphy was performed due to space limitation in the experimental setup. In introduction, Lietteri et. al have done shearing interferometry to gain quantitative information of density gradients along the nozzle flow. Inspired by this work, more information about fundamental properties of supercritical CO₂ phase change can be studied through an advanced non-intrusive measurement if granted an orthogonal optical access for a laser sheet. A PLIF or PIV measurement could be done on the flow field to resolve the velocity field of a nozzle flow.

5.2.3 Development of stochastic model in condensation behavior

From the characterization of the flow, a dominant frequency was obtained based on the nozzle geometry and a specific test section flow inlet conditions. It is suspected that these frequencies could be the key to explain the phenomena of vibrations and noise when operating a compressor with two-phase CO₂. The frequency when reaches the natural frequency of the overall system would definitely cause vibrations of the entire setup and lead to failure of components. More experiments will be conducted based on the nozzle profiles shown in Figure 22 and obtain dominant frequencies at different inlet conditions. A model should be developed that takes the nozzle geometry and inlet conditions to estimate the frequency of a suspected condensation behavior. This model can be utilized to predict condensation behavior on compressor blade leading edges where optical access is not present.

APPENDIX A. SAFETY OPERATING PROCEDURE

This appendix illustrates the steps in preparing and closing the experiment. The figure below lists the order of valves that need to be open before the experiment or closed after the experiment. This procedure is explained in CHAPTER 3, but this appendix provides further clarification using images.

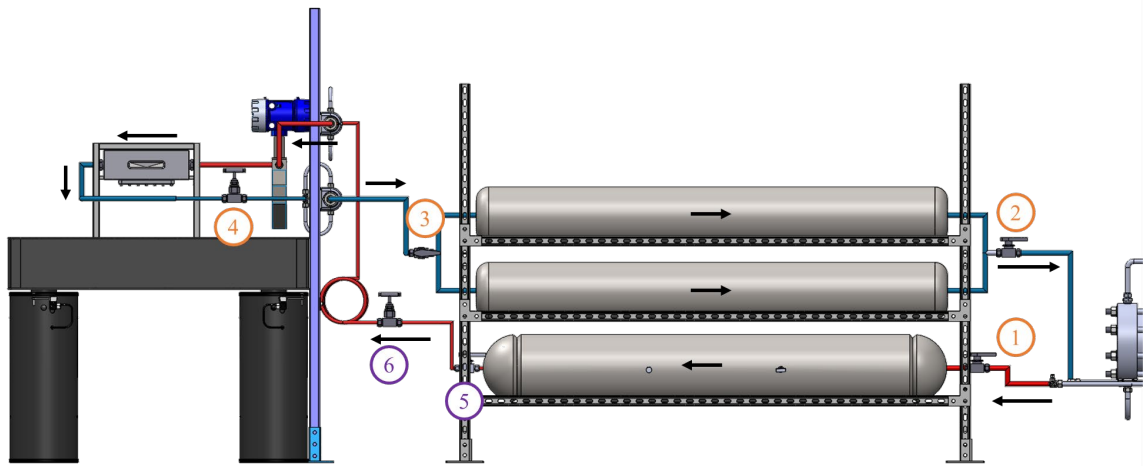


Figure 23: Order of valves opening before the experiment

Before the experiment, the valves need to be open in a sequential order listed in Figure 15 so that there is no pressure development that leads to a tube burst in the test loop assembly. Valves 5 and 6 are indicated in purple to show that these two valves can be opened once the compressor is started.

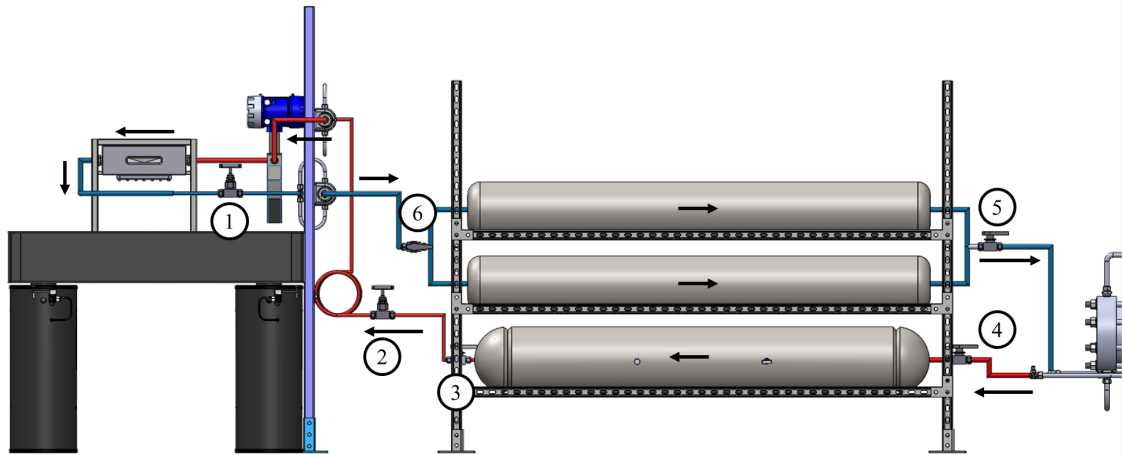


Figure 24: Order of valves closing after the experiment

These valves need to be sequentially closed so that there is not a section in the test loop where it remains highly pressurized other than the accumulators. The order eventually leads the high pressure CO₂ to be stored in the HP accumulator. Once the compressor is turned off, the LP accumulator is closed so that the two accumulators are isolated from the test section.

APPENDIX B. LIST OF LOOP COMPONENT SPECIFICATIONS

The facility components required high voltage and amperage ratings to maintain required power ratings. This appendix lists the specifications of the loop components.

- Hydropac CO₂ compressor
 - Electrical specification: 460 V, 3 Phase, 20 Amp
 - Motor power: 30 kW
 - Controlled type: Labview triggered step signal
 - Input voltage: 0 – 10 VDC
 - Cooling line requirement: 10 gallons per minute, 16 – 27 °C
- High-pressure accumulator heat jacket
 - Electrical specification: 240 V, 1 phase, 30 Amp
 - Controlled type: AC input solid state relay, pulse width signal
 - Input voltage: 240 V, switch controlled by Labview
- Pre-heater heat cartridge
 - Electrical specification: 10 kW, 480V, 1 Phase, 20 Amp
 - Controlled type: Labview triggered, AC input solid state relay, pulse width signal
 - Input voltage: 120V AC with K-type thermocouple analog signal

APPENDIX C. TUBE WALL THICKNESS CALCULATION

It is critical that the tube wall thickness meets the ASME pressure and vessel standard code. Thankfully, the system does not have extreme temperature that reduces the yield strength of the tube used. This appendix guides through the calculation of required minimum wall thickness using ASME standard code [22].

$$t_{min} = \frac{DP \cdot OD}{2AS \cdot JF + 2Y \cdot DP} + CA \quad (8)$$

Equation 8 is a process to calculate the minimum wall thickness for a straight pipe under internal pressure. Table 1 displays the values that are used for this experimental setup.

Table 3: minimum tube wall thickness calculation

Minimum wall thickness for a straight pipe under internal pressure		
T_{min}	minimum thickness (inch)	0.02595
DP	design pressure (psi)	1500
OD	outside diameter (in)	0.5
AS	allowable stress (psi)	17300
JF	joint factor	1
CA	corrosion allowance (in)	0.005
Y	wall thickness coefficient	0.4

From Table 3, the minimum thickness is 0.025. However, when performing maintenance or change in the loop design, 0.025" wall thickness tube deformed once applied Swagelok fitting. Considering the manufacturing tolerance and safety factor of 2.5, 0.065" wall thickness was used.

APPENDIX D. WINDOW WALL THICKNESS CALCULATION

To design an optically accessible window, a few types of glass are considered as a window material. Due to corrosive nature of CO₂ and a concern in scratches from a constant flow, sapphire glass window was selected. Compared to other types such as quartz or plastics such as plexiglas, sapphire had high compressive strength. This appendix tabulates necessary parameters to calculate minimum glass wall thickness using Equation 9. The minimum thickness when converted to inches was closed to 0.4 inch. To purchase an off-the-shelf product, 0.5" thickness of sapphire glass window was purchased.

$$T_{min} = 0.5L_w \left[\frac{K_w f_s \Delta P}{S_F} \right]^{0.5} \quad (9)$$

Table 4: minimum sapphire glass window wall calculation

Minimum wall thickness for a sapphire glass window		
T _{min}	minimum thickness (inch)	0.397
L _w	Unsupported length (mm)	138
K _w	Support condition constant	1.25
FOS	Factor of safety	4
dP	Pressure difference between P _{in} and P _o (MPa)	17.13
S _f	Fracture strength of material (MPa)	450

APPENDIX E. EXPERIMENTAL DATA

Table 5: Experimental data for Run #1 and #2

Case #	Pressure (MPa) at pressure port #										T (°C)		\dot{m} (kg/s)
	1	2	3	4	5	6	7	8	9	10	In	Out	
Case 1-1	7.426	error	7.432	7.381	7.321	7.239	7.232	7.29	7.297	7.314	31.26	30.38	0.056013
Case 1-1 Error	0.007465		0.009403	0.009073	0.00901	0.009386	0.009453	0.009322	0.009513	0.009527	2.2	2.2	0.0086
Case 1-2	7.397		7.401	7.354	7.305	7.225	7.22	7.277	7.283	7.292	31.52	30.25	0.049823
Case 1-2 Error	0.007821		0.009927	0.010415	0.008674	0.010114	0.008225	0.011655	0.009015	0.010291	2.2	2.2	0.0086
Case 2-1	7.480533	error	7.485867	7.4656	7.3536	7.313067	7.297067	7.409067	7.419733	7.429333	32.33	31.51	0.058279
Case 2-1 Error	0.006399		0.009117	0.010117	0.009528	0.010265	0.010556	0.009844	0.009283	0.009182	2.2	2.2	0.0086
Case 2-2	7.509333		7.5104	7.496533	7.399467	7.320533	7.296	7.399467	7.408	7.418667	32.39	31.43	0.061353
Case 2-2 Error	0.010056		0.011189	0.009822	0.013318	0.011321	0.008496	0.010417	0.011668	0.010462	2.2	2.2	0.0086

APPENDIX F. TEST SECTION AND HEATER ASSEMBLY

This appendix visualizes the test section and heater assembly. All the other test loop components are bought as off-the-shelf products. However, these two components are designed in-house and is custom manufactured. Figure 25 and Figure 26 show exploded views of the test section and the heater assembly respectively to aid the understanding of how these components are assembled.

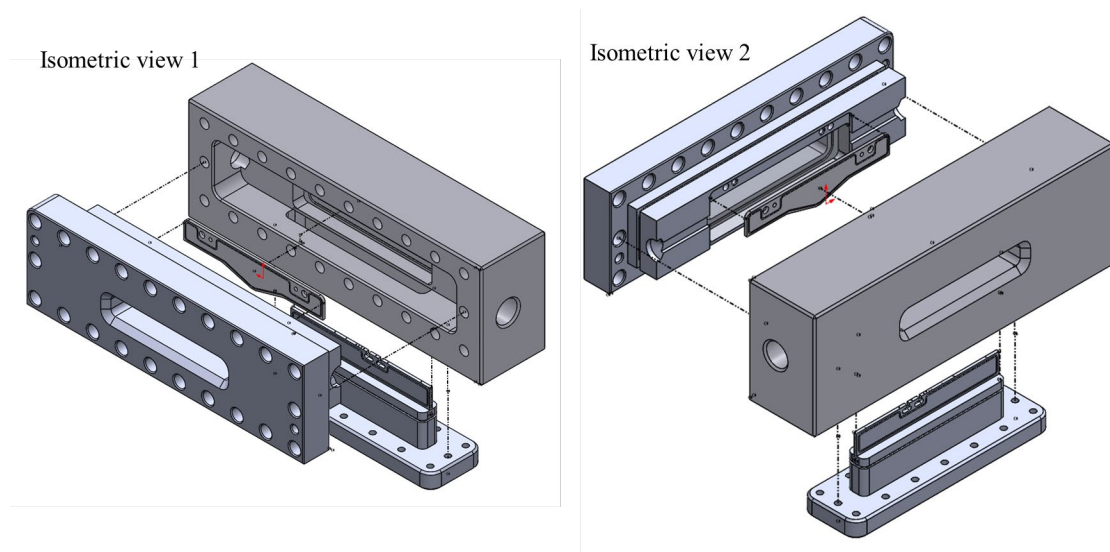


Figure 25: Exploded isometric view of test section

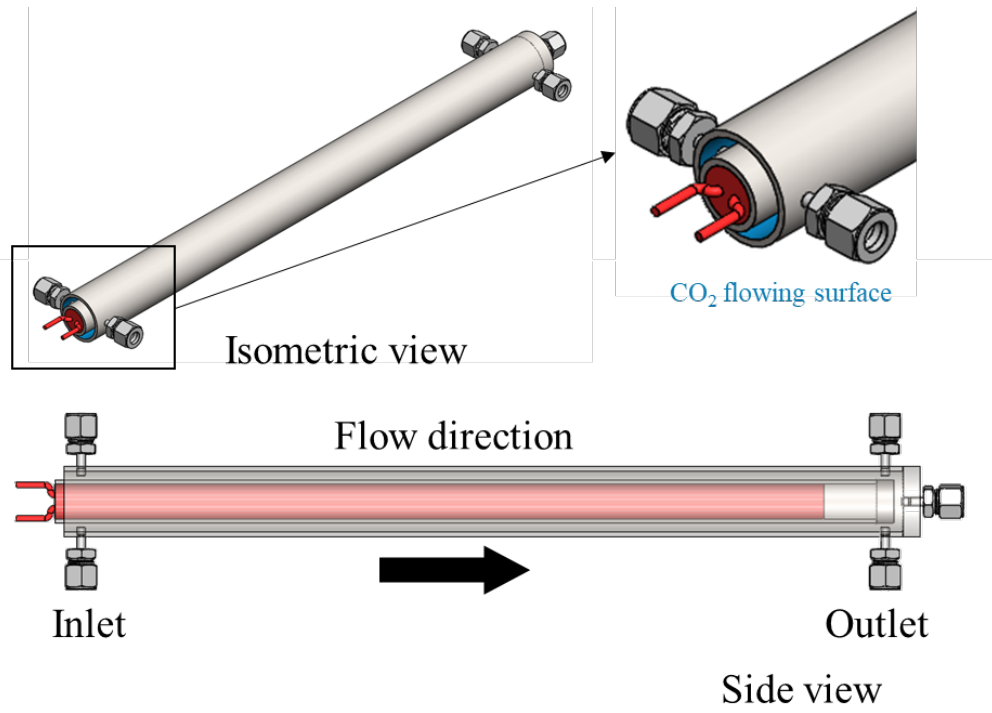


Figure 26: Isometric and side view of heater assembly

APPENDIX G. FLOW COEFFICIENT CALCULATION

A flow coefficient can be calculated based two different flow regime: subcritical flow and critical flow. These two flow regimes do not mean the fluid properties are beyond its critical point. These conditions indicate whether the flow is choked, and it is determined by the difference between upstream and downstream pressure of a valve. If the upstream pressure is greater than two times the downstream pressure, it is considered as a critical flow condition. Otherwise, it is considered as a subcritical flow condition. Equation 10, 11, and Table below summarizes the flow conditions and the valve location.

$$\text{Critical flow condition: } Cv = \frac{q\sqrt{SG \cdot T}}{816 \cdot P_1} \quad (10)$$

$$\text{Subcritical flow condition: } CV = \frac{q}{962} \sqrt{\frac{SG \cdot T}{P_1^2 - P_2^2}} \quad (11)$$

Table 6: Flow coefficient calculation for flow controlling valves

Model Number	SS-8GUF8	SS-5PDF8
Location	Outlet of high-pressure accumulator	Downstream of test section
Flow Condition	Critical	Subcritical
q (Flowrate), SCFH	7200	7200
P1 (Upstream Pressure), psia	2500	900
P2 (Downstream pressure), psia	1100	500
T(Temperature), °R	580	551.4
SG (Specific gravity of fluid)	1.529	1.529
CV (Flow coefficient)	0.105104	0.290403

Table 5 shows the corresponding flow coefficients. Referring to each flow coefficient chart, the needle valve is sufficient to set the upstream pressure and maintaining the flow rate.

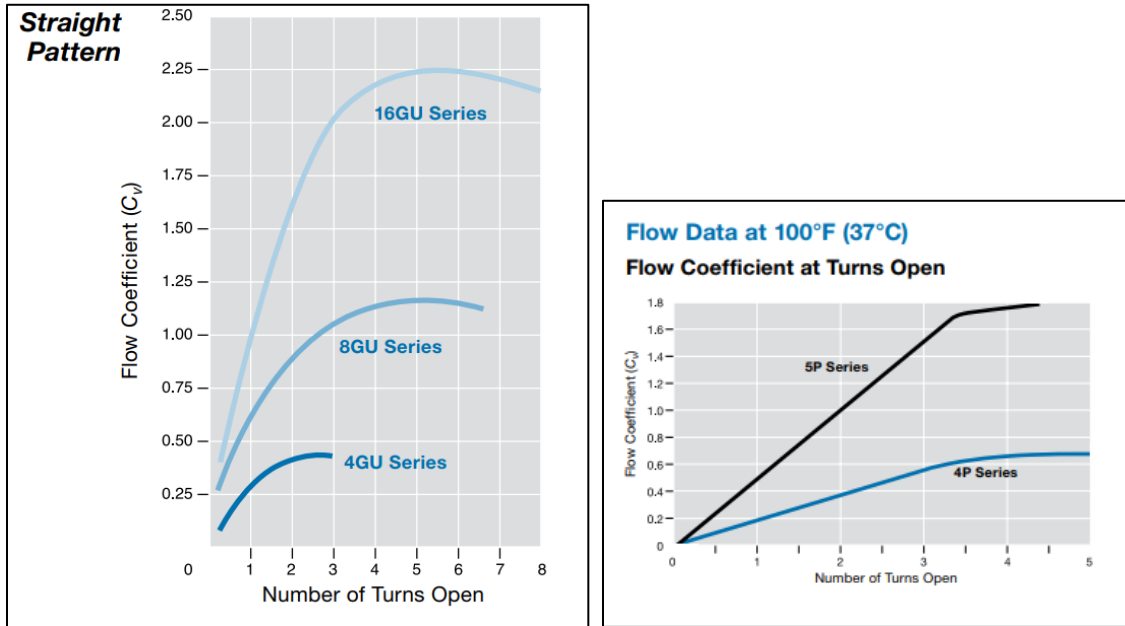
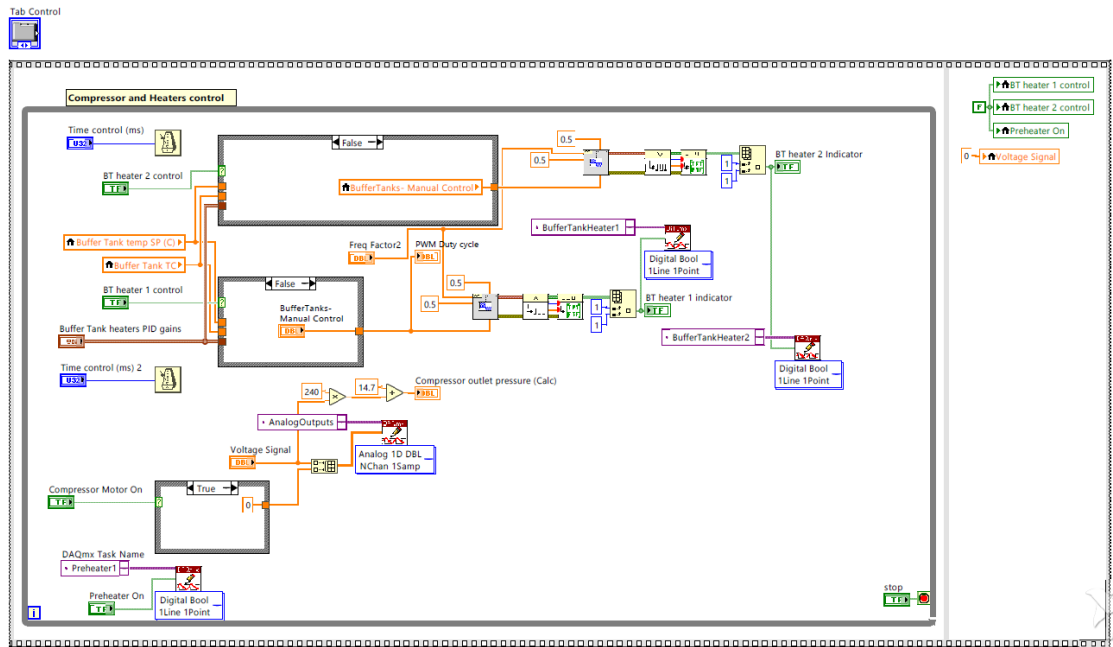


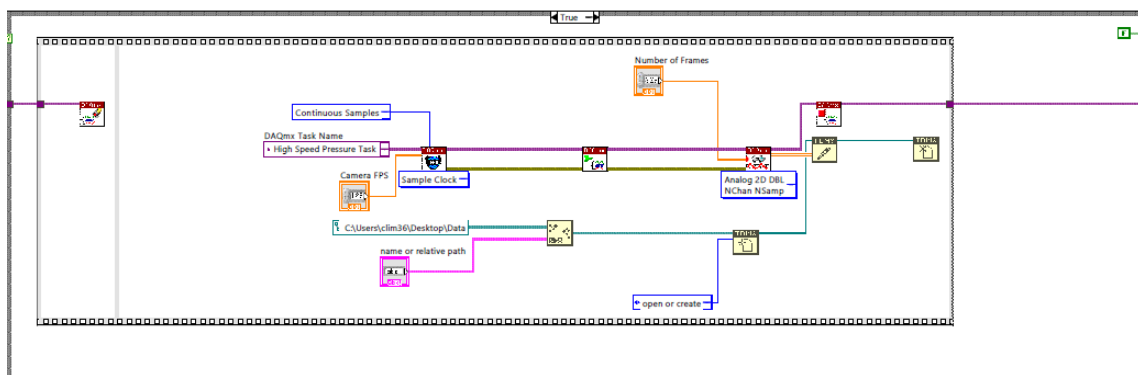
Figure 27: Flow coefficient chart for (left) SS-8GUF8 and (right) SS-5PDF8 [26], [27]

APPENDIX H. DATA ACQUISITION LABVIEW CODE

- Labview compressor and preheater controller block diagram



- Labview video sync data acquisition block diagram



-
- The screenshot displays the LabVIEW interface for the 'SPEED OF WHIRL LOOP' project. The front panel at the top includes a 'Camera Record' indicator, a 'false' status indicator, and a 'true' status indicator. The block diagram below shows the data acquisition and processing logic. It starts with an 'Analog Inputs Loop' that feeds into a 'Sample Clock' and 'Analog 10 DRL' block. This block outputs data to a 'Buffer Tank temp SP (C)' block, which then connects to a 'Buffer Tank temperature' block. The 'Buffer Tank temperature' block outputs various temperature and pressure data points to a 'Data Table'.
- The 'Data Table' contains the following data points:
- TS Inlet Temp
 - Test Section Temperature
 - TS outlet Temp
 - Reservoir Tank TC
 - Massflowrate
 - Buffer Tank TC
 - Buffer Tank temperature
 - Mdot (kg/s)
 - Cooler outlet TC
 - Buffer Tank Outlet TC
 - Density (kg/m³)
 - Upstream Tank Pressure
 - Downstream Tank Pressure
 - Buffer Tank pressure
 - TS Inlet Pressure
 - Test Section Pressure
 - TS Outlet Pressure
 - Compressor Outlet TC
 - Reservoir Tank pressure
 - TS Throat Pressure 1
 - TS Throat Pressure 2
 - Compressor Inlet TC

- EMERGENCY STOP**

Camera FPS: 1000.00

Number of Frames: 50

SPEED OF WHILE LOOP: 544

name or relative path: case1

rate: 10.00

sample mode: Continuous Samples

Acquisition data

Equipment Control | **Status Monitor** | **CNES Loop Diagram**

Low pressure buffer tank

Reservoir Tank TC: 10.4137

Reservoir Tank pressure: 960.832

Hydropac CO2 compressor

Compressor inlet TC: 17.0383

Compressor outlet pressure (Calc): 14.7

Compressor outlet TC: 17.2779

High pressure buffer tank

Buffer Tank pressure: 14.4272

Buffer Tank TC: 16.5597

Buffer Tank outlet TC: 18.8009

10kW cartridge heater

Flow control needle valve

Venturi test section

TS inlet Temp: 17.7414

TS outlet Temp: 17.77

TS Inlet Pressure: 15.4315

TS Outlet Pressure: 18.2879

Coriolis mass flow meter

Mdot (kg/s): 0.0046965

Density (kg/m³): 0.100241

Water Chiller

Water In

Cooler outlet TC: 17.2972

Water Out

Field of view

Flow direction

15.1817

17.0982

1.14

15.71°

10.56

1

2

3

4

5

6

7

TS Throat Pressure 2

TS Throat Pressure 1

NATIONAL INSTRUMENTS

LabVIEW - Home and Student Edition

APPENDIX I. CONDENSATION ANALYSIS USING MATLAB

- Condensation images processing using a reference image shown below

```
clc; clear; close all
Ref=imread('C:\Users\clim36\Desktop\Ref.tif');
picnum=10390; %12943
cond_xt=zeros(512,1024,1390);
pt1=[1000 375];
pt2=[1000 425];
i0=mean(Ref(pt1(2):pt2(2),pt1(1)));
i=1;
% for filenum=9001:10390
for filenum=9001:10390

    path=strcat('C:\Users\clim36\Desktop\DATA
IMAGES\102412\20180320_102412_C001H001S00010',num2str(sprintf('%05d',fi
lenum)),'.tif');
    Sample=imread(path);
    mm2px=0.04144;
    i1=mean(Sample(pt1(2):pt2(2),pt1(1)));
    Sample_rev=double(Ref)-double(Sample)*i0/i1;
    cond_xt(:,:,i)=Sample_rev;
%     if i>=1390
%         break;
end
    i=i+1;
end
```

- Reconstructing average condensation image shown below

```
AVG=zeros(512,1024);
for ii = 1:picnum
    AVG=AVG+cond_xt(:,:,ii);
end
AVGImg=AVG./picnum;
```

- Power spectral density code credit to Dr. Gokul Pathikonda at Georgia Institute of Technology

```
function [f,Y] = myPSD(t,S,seglength,overlap)
% Written by Gokul Pathikonda (2012)
% This program computes PSD of a time signal S at times t (equally
spaced)
% Inputs:
% t = times (Eg: t = [0,0.1,0.2,0.3]); HAS To be equal intervals
% S = signal at time steps for which PSD has to be computed
```



```

% seglength = (optional) length of segments the main signal needs to be
cut into for welching.
%           this as powers of 2 for FFT to work best. If this is
not
%           specified, full signal PSD is taken,
% overlap = (optional) fraction overlap, 0.5 if not specified
% Outputs: (Both of length next power of seglength)
% f = frequency axis corresponding to the times provided
% Y = PSD signal

t = t(:);
S = S(:);

% Fill the NaNs with interpolation if any;
NaNIndices = find(isnan(S));
NoNaNIndices = find(~isnan(S));
if ~isempty(NaNIndices)
    warning('NaNs found and values interpolated');
    S(NaNIndices) = interp1(t(NoNaNIndices), S(NoNaNIndices),
t(NaNIndices));
end

if nargin == 2
    seglength = length(S);
    overlap = 0.5;
elseif nargin == 3
    overlap = 0.5;
end

if mod(seglength,1) ~=0 || seglength <= 0
    error('''seglength'' has to be a whole number');
end

% if seglength < 3000
%     warning('Seglength too small. Windowing may be poorly
conditioned')
% end

Fs = 1/(t(2) - t(1));

% no_max = floor(2*length(S)/seglength-1);
no_max = floor((length(S)-seglength)/(seglength*(1-overlap))+1);

w = hann(seglength, 'periodic');
% w = 1;

NFFT = 2^nextpow2(seglength);
f = 0:Fs/NFFT:Fs/2;
f = f';
Y = zeros(NFFT/2+1,1);
Multiplier = zeros(no_max,1); % to adjust for energy lost due to
windowing
PartStart = floor(seglength*(1-overlap));
for i = 1:no_max

```

```

%     PartSignal = S(((seglength/2)*(i-1)+1):((seglength/2)*(i-1) +
seglength));
%     if i == no_max
%         pause(1)
%     end
    PartSignal = S((PartStart*(i-1)+1):(PartStart*(i-1) + seglength));
    Seg = w.*PartSignal;
    Multiplier(i) = var(PartSignal)/var(Seg);
    xdft = fft(Seg,NFFT);
    xdft = xdft(1:NFFT/2+1);
    psdx = Multiplier(i)*(1/(Fs*seglength)).*abs(xdft).^2;
    psdx(2:end-1) = 2*psdx(2:end-1);
    Y = Y + psdx;
%     var(PartSignal)/trapz(f,psdx)
end
% if (mean(Multiplier) < 2.6) || (mean(Multiplier) > 2.75) ||
(max(Multiplier) > 5) || (max(Multiplier) < 1.5)
%     warning('Windowing might be poorly conditioned for the given
seglength')
%     disp(strcat('Mean multiplier: ', num2str(mean(Multiplier))));
%     disp(strcat('Max multiplier: ', num2str(max(Multiplier)),'; Min
multiplier: ',num2str(min(Multiplier))));
% end
Y = Y/(no_max);

f = f(2:end); % Removing zeroth frequency
Y = Y(2:end);

end

```

Plotting power spectral density for each graph

```

Ref=imread('C:\Users\clim36\Desktop\Ref.tif');
FOVMask = (Ref>200);
Corr_cond_xt =
(cond_xt)./repmat(double(Ref),1,1,3000).*repmat(FOVMask,1,1,3000);
CondSum = nansum(nansum(Corr_cond_xt));
CondSum = permute(CondSum,[3,2,1]);
CondSum = CondSum./sum(FOVMask(:));
line1 = [332:440,400];
lineavgts1 = permute(nanmean(ss1(y>349&y<436,400,:),1),[3,2,1]);
lengthS=60;
[f1,phil]=myPSD(t,lineavgts1-mean(lineavgts1),lengthS);
linelavg = mean(AVGImg(349:436,400))^2;
linelvar = mean(var(349:436,400));
semilogx(f1.*42748./5469.8,f1.*phil*linelvar)

```

APPENDIX J. HOMOGENEOUS EQUILIBRIUM MODEL CODE

```
% Input parameters %
lambda=0.582; % Wavelength of laser beam in micrometer %
fluid='CO2';
% P_inlet=7.4; % Inlet pressure in MPa %
% T_inlet=31.4; % Inlet temperature in C %
% mdot=0.03; % Mass flow rate in kg/s %
P_inlet=7.5; % Inlet pressure in MPa %
T_inlet=32; % Inlet temperature in C %
mdot=0.033; % Mass flow rate in kg/s %
width=3; % Width of channel in mm %
height_inlet=1.058; % Height of nozzle at inlet in cm %
height_throat=0.1; % Height of nozzle at throat in cm %
% Converging_radius=1.008; % Radius of converging section in cm %
height_outlet=1.058;
Length_throat=0.5; % Length of throat in cm %
Develop_length=4.27; % Length of developing region in cm %
Total_length=16.3; % Total length of venturi profile in cm %
epsilon=3.8*10^-6; % Surface roughness in m %
g_acc=9.81; % Gravitational acceleration - m/s^2 %
theta=90; % Direction of flow with respect to gravity %
correlation=2; % Friction factor correlation - choose 1 for Blasius
correlation, 2 for Colebrook correlation %
plots=0; % 1 for true and 0 for false %
A_inlet=(width/1000)*(height_inlet/100); % Inlet area in m^2 %
A_throat=(width/1000)*(height_throat/100); % Throat area in m^2 %
[rho_inlet,h_inlet,Cp_inlet,mu_inlet,Cond_inlet,Pr_inlet,s_inlet] =
REFPROP_TP(P_inlet,T_inlet,fluid); % Thermo-physical properties @ inlet
%
z_start=0; % Start of venturi profile in cm %
z_end=Total_length; % End of venturi profile in cm %
N_nodes=1000; % Number of discretization nodes %
dz=(z_end-z_start)/(N_nodes-1);
Rindex_ref=1+6.991*10^(-2)/(166.175-lambda^(-2))+1.4472*10^(-
3)/(79.609-lambda^(-2))+6.42941*10^(-5)/(56.3064-lambda^(-
2))+5.21306*10^(-5)/(46.0196-lambda^(-2))+1.46847*10^(-6)/(0.0584738-
lambda^(-2)); % Refractive index at reference conditions %
P_ref=101.325; % Reference pressure in kpa %
T_ref=273.15; % Reference temperature in kpa %
T_0 = 17; % Room Temperature
rho_ref=refpropm('D','T',T_ref,'P',P_ref,fluid);
LL_constant=(Rindex_ref^2-1)/(rho_ref*(Rindex_ref^2+2)); % Lorentz-
Lorentz constant %

z=zeros(1,N_nodes);
height=zeros(1,N_nodes);
x=zeros(1,N_nodes);
rho=zeros(1,N_nodes);
h=zeros(1,N_nodes);
Qual=zeros(1,N_nodes);
void_frac=zeros(1,N_nodes);
soundspeed=zeros(1,N_nodes);
Mach=zeros(1,N_nodes);
```

```

Rindex=zeros(1,N_nodes);
mu=zeros(1,N_nodes);
P=zeros(1,N_nodes);
S=zeros(1,N_nodes);
T=zeros(1,N_nodes);
U=zeros(1,N_nodes);
irrev=zeros(1,N_nodes);
Dh=zeros(1,N_nodes);
mu_avg=zeros(1,N_nodes-1);
rho_avg=zeros(1,N_nodes-1);
Re=zeros(1,N_nodes-1);
Dh_avg=zeros(1,N_nodes-1);
G=zeros(1,N_nodes-1);
deltaP_fric=zeros(1,N_nodes-1);
deltaP_acc=zeros(1,N_nodes-1);
deltaP_grav=zeros(1,N_nodes-1);
f=zeros(1,N_nodes-1);

U_inlet=mdot/(A_inlet*rho_inlet);
U(1)=U_inlet;
P(1)=P_inlet;
T(1)=T_inlet;
S(1)=s_inlet;
[rho(1),h(1),~,mu(1),~,~,~] = REFPROP_TP(P(1),T(1),fluid); % Thermo-
physical properties at nodes %
Qual(1)=refpropm('Q','P',P(1)*1000,'H',h(1),fluid);

% Fabricated profile %
for i=1:N_nodes
    x(i)=Total_length*i/N_nodes;
    if (x(i)<=4.274) || (x(i)>12.026)
        height(i)=1.058;
    elseif (x(i)> 4.274) && (x(i)<= 7.9)
        height(i)=1.058+(1.16-10.58)/(36.26)*(x(i)-4.274);
    elseif (x(i)> 7.9) && (x(i)<=8.4)
        height(i) = 0.116;
    elseif (x(i)>8.4) && (x(i)<=12.026)
        height(i) = 0.116+(10.58-1.16)/(36.26)*(x(i)-8.4);
    end
    Dh(i)=4*(width/1000)*(height(i)/100)/(2*width/1000+2*height(i)/100);
% Hydraulic diameter - in m, 4*Ac/P %
end

P(1)=P_inlet;
h(1)=h_inlet;
% Isentropic Homogeneous equilibrium model %
for i=1:N_nodes-1
    P(i+1)=0.99*P(i); % Guess values for next node pressure and
enthalpy %
    h(i+1)=0.99*h(i);
    for j=1:100
        P_out_old=P(i+1);
        h_out_old=h(i+1);
        Qual(i+1)=refpropm('Q','P',P(i+1)*1000,'H',h(i+1),fluid);
        if (Qual(i+1)<1) && (Qual(i+1)>0)
            mu_l=refpropm('V','P',P(i+1)*1000,'Q',0,fluid);

```

```

mu_g=refpropm('V','P',P(i+1)*1000,'Q',1,fluid);
mu(i+1)=power((Qual(i+1)/mu_g+(1-Qual(i+1))/mu_l),-1);
rho_l=refpropm('D','P',P(i+1)*1000,'Q',0,fluid);
rho_g=refpropm('D','P',P(i+1)*1000,'Q',1,fluid);
rho(i+1)=power((Qual(i+1)/rho_g+(1-Qual(i+1))/rho_l),-1);

else
    mu(i+1)=refpropm('V','P',P(i+1)*1000,'H',h(i+1),fluid);

rho(i+1)=refpropm('D','P',P(i+1)*1000,'H',h(i+1),fluid);
end

G(i)=mdot/((width/1000)*(height(i)/100));
G(i+1)=mdot/((width/1000)*(height(i+1)/100));
Re(i)=G(i)*Dh(i)/mu(i);
Re(i+1)=G(i+1)*Dh(i+1)/mu(i+1);
f(i)=frictionfactor(Re(i),epsilon,correlation);
f(i+1)=frictionfactor(Re(i+1),epsilon,correlation);

deltaP_fric(i)=(dz/100)*0.5*(f(i)*G(i)^2/(2*rho(i)*Dh(i))+f(i+1)*G(i+1)^2/(2*rho(i+1)*Dh(i+1))); % Frictional pressure drop %
deltaP_acc(i)=(G(i+1)^2/rho(i+1)-G(i)^2/rho(i)); % acceleration pressure drop %

deltaP_grav(i)=dz*0.5*(rho(i)+rho(i+1))*g_acc*cos(theta*pi/180); % Gravitational pressure drop %
P(i+1)=P(i)-(deltaP_fric(i)+deltaP_acc(i)+deltaP_grav(i))/10^6;
% Pressure at the next nodes %
if P(i+1) < 0
    P(i+1)=0.99*P(i);
end
U(i+1)=G(i+1)/rho(i+1);
h(i+1)=h_inlet+U_inlet^2/2-U(i+1)^2/2;
Qual(i+1)=refpropm('Q','P',P(i+1)*1000,'H',h(i+1),fluid);
T(i+1)=refpropm('T','P',P(i+1)*1000,'H',h(i+1),fluid)-273.15;
S(i+1)=refpropm('S','P',P(i+1)*1000,'H',h(i+1),fluid);
irrev(i+1)=T_0*(S(i+1)-S(i))-(h(i+1)-h(i))-(U(i+1)-U(i))^2/2;
if (Qual(i+1)<1) && (Qual(i+1)>0)
    mu_l=refpropm('V','P',P(i+1)*1000,'Q',0,fluid);
    mu_g=refpropm('V','P',P(i+1)*1000,'Q',1,fluid);
    mu(i+1)=power((Qual(i+1)/mu_g+(1-Qual(i+1))/mu_l),-1);
    rho_l=refpropm('D','P',P(i+1)*1000,'Q',0,fluid);
    rho_g=refpropm('D','P',P(i+1)*1000,'Q',1,fluid);
    rho(i+1)=power((Qual(i+1)/rho_g+(1-Qual(i+1))/rho_l),-1);

else
    mu(i+1)=refpropm('V','P',P(i+1)*1000,'H',h(i+1),fluid);

rho(i+1)=refpropm('D','P',P(i+1)*1000,'H',h(i+1),fluid);
end

if (abs((P(i+1)-P_out_old))<=1e-6 && abs((h(i+1)-h_out_old))<=1e-6)
    break;
end

```

```

        end
    end

% Post processing of the data - calculation of void fraction and speed
of sound %
for i=1:N_nodes

    if Qual(i)>1 || Qual(i)<0
        Qual(i)=1;
        void_frac(i)=1;
        soundspeed(i)=refpropm('A','P',P(i)*1000,'H',h(i),fluid);
    elseif Qual(i)>=0 && Qual(i)<=1
        rho_l=refpropm('D','P',P(i)*1000,'Q',0,fluid);
        rho_g=refpropm('D','P',P(i)*1000,'Q',1,fluid);
        soundspeed_l=refpropm('A','P',P(i)*1000,'Q',0,fluid);
        soundspeed_g=refpropm('A','P',P(i)*1000,'Q',1,fluid);
        void_frac(i)=1/(1+((1-Qual(i))/Qual(i))*(rho_g/rho_l));
        soundspeed(i)=(rho_l*(1-
void_frac(i))+rho_g*void_frac(i))*(void_frac(i)/(rho_g*soundspeed_g^2)+
(1-void_frac(i))/(rho_l*soundspeed_l^2))^(-0.5);
    end
    Mach(i)=U(i)/soundspeed(i);
    Rindex(i)=power((3/(1-LL_constant*rho(i))-2),0.5);

end

```

APPENDIX K. NOZZLE DIMENSIONS

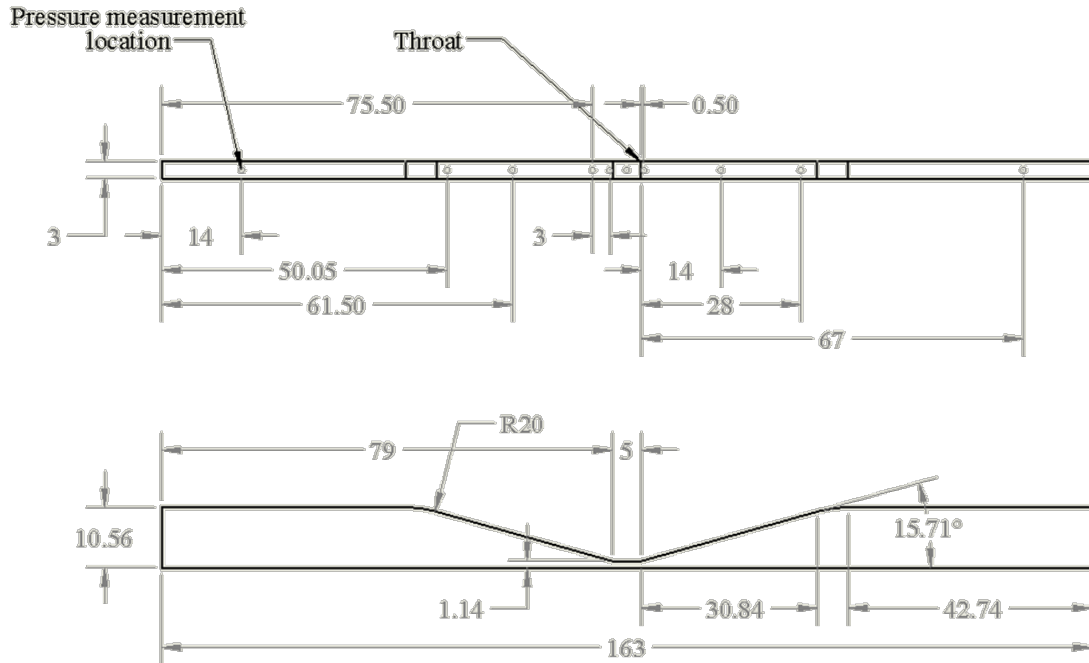


Figure 28: Nozzle dimensions and locations of pressure transducers

APPENDIX L. IMPROVEMENTS TO THE FACILITY

After assembling the loop, there were issues in collecting meaningful data. This appendix explains three biggest issues present when assembling the loop the solutions to the problem.

1. Volume

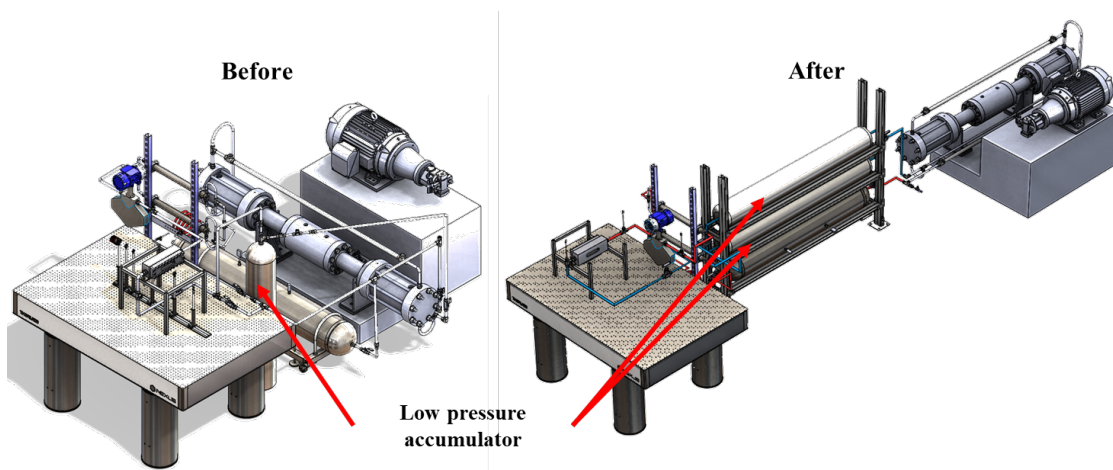


Figure 29: (Left) Previous experimental setup with 5 gallons of LP accumulator (Right) current experimental setup with 30 gallons of LP accumulator

Because the compressor used in this study was a positive displacement compressor, there was an inherent pressure fluctuation. This is also mentioned in flow control equipment section. Due to the flow rate fluctuation, the system required more volume to be added at the upstream of the test section. Because at the downstream of the compressor, there was a HP accumulator present, it was suspected that addition of more volume at the upstream of the compressor would solve the issue, as this facility is a closed-loop with all the components connected in series. Figure 29 shows the previous experimental setup and its modification. LP accumulator was only 5 gallon, leading to a huge flow fluctuation

when the compressor was drawing out CO₂ from upstream. Thus, more volume was added by replacing with two 15-gallon carbon steel tanks. This definitely mitigated the flow fluctuations and no sensible oscillating phase transition behavior was shown in the test section.

2. Sealing

Test section flanges form a rectangular converging-diverging channel. These flanges come in contact with the sapphire windows in the test section. Contact between metal and glass surface leads to crack of sapphire glass windows and leakage of CO₂ in the test section at high-pressure conditions. Thus, o-ring grooves are machined on to the flange that come in contact with the sapphire glass window. Due to geometric constraints of flanges, 0.8 mm o-ring grooves are machined on the flanges to allow Viton 1 mm o-ring. Figure 30 shows modifications of these flanges.

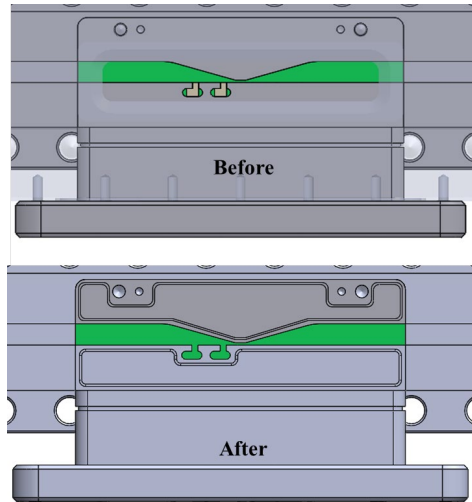
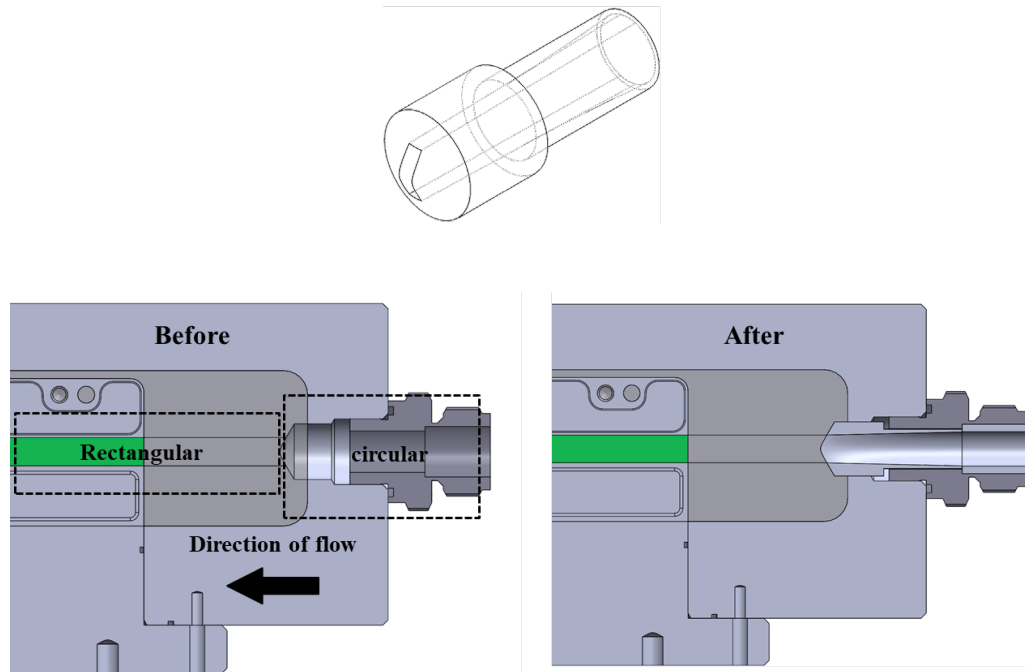


Figure 30: Front views of test section flanges before and after o-ring groove installation

3. Flow transition

Flow profile inside the test section is a rectangular cross section. However, CO₂ coming inside the test section has a circular cross section. Because there is no smooth transition from circular to rectangular cross-section, phase transition behavior is unstable when running experiments. To deduce a statistically stationary information from a turbulent flow, guidance insert is machined using a stainless steel 304 rod to provide a smooth transition between circular cross section to rectangular cross section. The image of the flow guidance insert and an image of its installation in the test section can be found in Figure 31.



**Figure 31: (Top) Wire diagram of the flow guidance insert
(Bottom) Test section inlet cross-sectional image of before and after installation of
flow guidance insert**

REFERENCES

- [1] Ahn, Yoonhan, Seong Jun Bae, Minseok Kim, Seong Kuk Cho, Seungjoon Baik, Jeong Ik Lee, and Jae Eun Cha. "Review of supercritical CO₂ power cycle technology and current status of research and development." *Nuclear Engineering and Technology* 47, no. 6 (2015): 647-661.
- [2] Gibbins, Jon, and Hannah Chalmers. "Carbon capture and storage." *Energy policy* 36, no. 12 (2008): 4317-4322.
- [3] US Department of Energy. "Enhanced Oil Recovery." *Energy.Gov*. <https://www.energy.gov/fe/science-innovation/oil-gas-research/enhanced-oil-recovery>.
- [4] Dostál, V., M. J. Driscoll, and P. Hejzlar. "A Supercritical Carbon Dioxide Cycle for Next Generation Nuclear Reactors." PhD diss., Massachusetts Institute of Technology. 2004. <https://dspace.mit.edu/handle/1721.1/17746>
- [5] Chaitanya Vishwajit Halbe. "Effects of Two-Phase Flow in a Multistage Centrifugal Compressor." PhD diss., Virginia Institute of Technology. 2016. <https://vtechworks.lib.vt.edu/handle/10919/73305>
- [6] Duff, Karl Melton. "Non-equilibrium condensation of carbon dioxide in supersonic nozzles." PhD diss., Massachusetts Institute of Technology. 1966. <https://dspace.mit.edu/handle/1721.1/13416>
- [7] Lettieri, Claudio, Derek Paxson, Zoltan Spakovszky, and Peter Bryanston-Cross. "Characterization of Nonequilibrium Condensation of Supercritical Carbon

- Dioxide in a de Laval Nozzle." *Journal of Engineering for Gas Turbines and Power* 140, no. 4 (2018): doi:10.1115/1.4038082.
- [8] Lettieri, C., D. Yang, and Z. Spakovszky. "An investigation of condensation effects in supercritical carbon dioxide compressors." *Journal of Engineering for Gas Turbines and Power* 137, no. 8 (2015): 082602.
- [9] Span, Roland, and Wolfgang Wagner. "A new equation of state for carbon dioxide covering the fluid region from the triple-point temperature to 1100 K at pressures up to 800 MPa." *Journal of physical and chemical reference data* 25, no. 6 (1996): 1509-1596.
- [10] Liu, Fang, Eckhard A. Groll, and Daqing Li. "Investigation on performance of variable geometry ejectors for CO₂ refrigeration cycles." *Energy* 45, no. 1 (2012): 829-839. <https://doi.org/10.1016/j.energy.2012.07.008>.
- [11] Nakagawa, Masafumi, Menandro Serrano Berana, and Akinori Kishine. "Supersonic two-phase flow of CO₂ through converging–diverging nozzles for the ejector refrigeration cycle." *international journal of refrigeration* 32, no. 6 (2009): 1195-1202. ISSN 0140-7007, <https://doi.org/10.1016/j.ijrefrig.2009.01.015>.
- [12] Hosangadi, Ashvin, Zisen Liu, Timothy Weathers, Vineet Ahuja, and Judy Busby. "Modeling Multi-Phase Effects in CO₂ Compressors at Subcritical Inlet Conditions." *Journal of Engineering for Gas Turbines and Power* (2019).
- [13] Hosangadi, A., T. Weathers, Z. Liu, V. Ahuja, and J. Busby. "Numerical Simulations of CO₂ Compressors at Near-Critical and Sub-Critical Inlet Conditions." In *ASME Turbo Expo 2018: Turbomachinery Technical Conference*

- and Exposition, pp. V009T38A002-V009T38A002. American Society of Mechanical Engineers, 2018.
- [14] Ameli, Alireza, Ali Afzalifar, Teemu Turunen-Saaresti, and Jari Backman. "Centrifugal Compressor Design for Near-Critical Point Applications." *Journal of Engineering for Gas Turbines and Power* 141, no. 3 (2019): 031016.
 - [15] Jarrahbashi, Dorrin, S. R. Pidaparti, and Devesh Ranjan. "Nucleation of supercritical carbon dioxide in a venturi nozzle." *Nuclear Engineering and Design* 310 (2016): 69-82. <https://doi.org/10.1016/j.nucengdes.2016.09.022>.
 - [16] Paxon, Derek Edwin. "Experimental Characterization of Condensation Behavior for Metastable Carbon Dioxide." MS Thesis., Massachusetts Institute of Technology. 2016. <https://dspace.mit.edu/handle/1721.1/107053>
 - [17] Reboud, Jean-Luc, Benoit Stutz, and Olivier Coutier. "Two phase flow structure of cavitation: experiment and modeling of unsteady effects." In *3rd International Symposium on Cavitation CAV1998*, Grenoble, France, vol. 26. 1998.
 - [18] Mauger, Cyril, Loïc Méès, Marc Michard, Alexandre Azouzi, and Stéphane Valette. "Shadowgraph, Schlieren and interferometry in a 2D cavitating channel flow." *Experiments in fluids* 53, no. 6 (2012): 1895-1913.
 - [19] Chen, G. H., G. Y. Wang, C. L. Hu, B. Huang, and M. D. Zhang. "Observations and measurements on unsteady cavitating flows using a simultaneous sampling approach." *Experiments in Fluids* 56, no. 2 (2015): 32.
 - [20] Ushifusa, Hiroyuki, Kazuaki Inaba, Konosuke Sugawara, Kosuke Takahashi, and Kikuo Kishimoto. "Measurement and visualization of supercritical CO₂ in dynamic

- phase transition." In EPJ Web of Conferences, vol. 92, p. 02103. EDP Sciences, 2015.
- [21] Okamoto, Koji, Jun Ota, Katsumi Sakurai, and Haruki Madarame. "Transient velocity distributions for the supercritical carbon dioxide forced convection heat transfer." *Journal of nuclear science and technology* 40, no. 10 (2003): 763-767.
 - [22] ASME, 2016, "ASME B31.1-2016 Edition, Power Piping," ASME Code for Pressure Piping, B31, An American National Standard, The American Society of Mechanical Engineers, New York., NY.
 - [23] Ghiaasiaan, S. Mostafa. Two-phase flow, boiling, and condensation: in conventional and miniature systems. Cambridge University Press, 2007.
 - [24] Cognata, Thomas J., D. Keith Hollingsworth, and Larry C. Witte. "High-speed visualization of two-phase flow in a micro-scale pin-fin heat exchanger." *Heat Transfer Engineering* 28, no. 10 (2007): 861-869.
 - [25] Smith, Charles Robert, and Stephen Jay Kline. "An experimental investigation of the transitory stall regime in two-dimensional diffusers." *Journal of Fluids Engineering* 96, no. 1 (1974): 11-15.
 - [26] Swagelok, 2017, "General Utility Service Needle Valves-GU series," MS-02-312, R7, October 2017. Page 3. Swagelok Company, Solon, Ohio.
 - [27] Swagelok, 2017, "Rising Plug Valve- 4P and 5P Series," MS-01-49, R13, October 2017. Page 3. Swagelok Company, Solon, Ohio.